Light Emission Measurements on Diodes

2016

M.Sc. thesis

Aristotelis Karavidas

University of Twente
Department of Electrical Engineering,
Mathematics & Computer Science (EEMCS)
Semiconductor Components Group (SC)

Enschede,
The Netherlands

Contents

Figure list

Abstract

The goal of this assignment was the development of a measurement tool for synchronized electrical and optical analysis of opto-electronic devices. This is beneficial for automated characterization of opto-electronic devices and thus, expand our knowledge on the optical behavior of devices. The communication between two basic instruments is used for this purpose: Keithley 4200 SCS for electrical characterization and a camera from XENICS for optical imaging (visible range: XEVA-257, infra-red range: XEVA-320 InGaAs). These two instruments communicate through semaphores. Measurements were carried out on various devices to confirm the operation of the tool. The optical behavior of ultra-shallow vertical p^+n junctions with V_{BR}=7V in avalanche-mode was investigated with the tool. In particular, based on the available knowledge of the processing and current-voltage characteristics of the diodes a certain amount of defects in the n-silicon region were expected. Spatially invariant photon-emission spots from the active area with repeated avalanche-mode biasing indicate that the origin of the spots is in fact connected to the defect-density in the material. The spot-count and hence, total intensity increases with increasing bias, which matches results with prior literature. The number of spots increases in circular diodes with bigger diameters (due to higher active area). The intensity, however, increases for diodes with decreasing diameter, at a given bias. The automation also enables us to record the variation in optical behavior of similar structures on multiple locations of the wafer, which provides greater insight about the level of uncertainty in the fabrication process throughout the wafer. The electro-luminescence of the diodes is also observed in forward bias. The infra-red emission shows a peripheral glow around the diode. Diodes with break-down voltage of 14 V also show a peripheral glow around the diode in the visible range in avalanche-mode. Uniform light emission is obtained in forward bias for the same diode. Series resistance and current components (peripheral and areal) are calculated in order to discuss and support the origin of these observations.

1. Introduction

There exist various kinds of luminescence (emission of photons) which are classified based on the type of excitation mechanism such as: photoluminescence, cathodoluminescence, radio-luminescence and electroluminescence. Our focus will be on electroluminescence. Electroluminescence is the emission of light from a material when excited by electron injection. A photon is emitted in the process when an electron and a hole recombine, and some fraction of the energy is released radiatively. Electro-luminescence can be caused by injection currents, avalanche breakdown and carrier tunneling. Light Emitting Diode (LED) is a common electro-luminescent device which basically consists of a p-n junction. By applying a forward bias, minority carriers are injected to the junction. A fraction of electron-hole pairs undergo radiative recombination, and hence emit photons.

Silicon (Si) is widely used for the fabrication of optical waveguides and filters. It is, however, not preferred as a material for light emitting devices due to its indirect band gap. Its band-gap of 1.12 eV at 300 K leads to infrared light emission upon being excited in forward bias, which stimulates inter-band recombination. This however, occurs at a very low efficiency, since a significant fraction of the transition energy is transferred to phonons. Avalanche-mode Si LEDs however, emit light within the visible range **[1], [2].** Avalanche breakdown is a phenomenon which occurs due to collision of charge carriers with the Si lattice. These collisions (impact ionization) produce electron-hole pairs which under the influence of sufficiently high applied electric field, are able to sustain the chain of the ionization process. This carrier multiplication increases the current by a few orders of magnitude, with a very small change in bias voltage. EHPs (Electron-Hole Pairs) are accelerated to higher energies ($>1.5E_g$) in this process. When some of them make a transition to VB (Valence Band) the photons of shorter wavelengths are emitted by Si diodes in avalanche-mode. Emission appears as spots scattered along the diode near the metallurgical junction. A vertical ultra-shallow p^+n junction diode **[3]**, **[4]**, **[16]** which emits infra-red light in forward bias and visible light in reverse bias (avalanche- mode) is the device under test (DUT) in this report.

The connection between electrical and optical behavior of electro-luminescent devices is generally important for a detailed study. Synchronized electrical and optical measurements are necessary for analysis and comparison. This synchronization can be practically implemented with a proper setup and programming. Semaphores are special data-types suitable for multi-threaded programming environment, which can be used for the synchronized acquisition of optical and electrical data. A camera and electrical characterization equipment can be synchronized with semaphores. This implementation was used in this project in order to capture synchronized electrical and optical data and provide more physical insight on the opto-electronic behavior of the DUT.

Two basic areas of interest exist in this assignment: the development of an electro-optical analysis tool and the confirmation of its operation through measurements on opto-electronic devices. This tool consists of a Keithley 4200 SCS and a camera from XENICS for optical imaging (visible range: XEVA-257, infra-red range: XEVA-320 InGaAs). The programming interface used for the implementation of the tool is Visual C and C++ IDE. Two processes were developed: the electrical characterization (written in C) and camera process (written in C++). These two processes are synchronized through semaphores. The main aim of the experimental work done in this project was to investigate the optical response of the avalanche-mode Si diode. The programming and diode measurements are analyzed in separate chapters within this report.

In the second chapter, the setup structure is described. In the third chapter, a few important electrical and optical properties of Si are mentioned. In the fourth chapter, the structure of the diode is analyzed. In the fifth chapter, the experiments that were carried out are explained. In the sixth chapter, the results which were obtained from the experiments are analyzed. Next, a discussion on the results follows which ends with the conclusions.

2. Setup description: software and hardware

The build of the setup is an important part of this assignment. Two instruments were used for this purpose, an electrical characterization machine: Keithley 4200 SCS and a camera: InGaAs XEVA 257 or 320. They are connected with USB (Universal Serial Bus). USB was not the first way selected for their connection. A lot of options were considered at the beginning of the design based on the specifications of the equipment. These options are shown at figure 1:

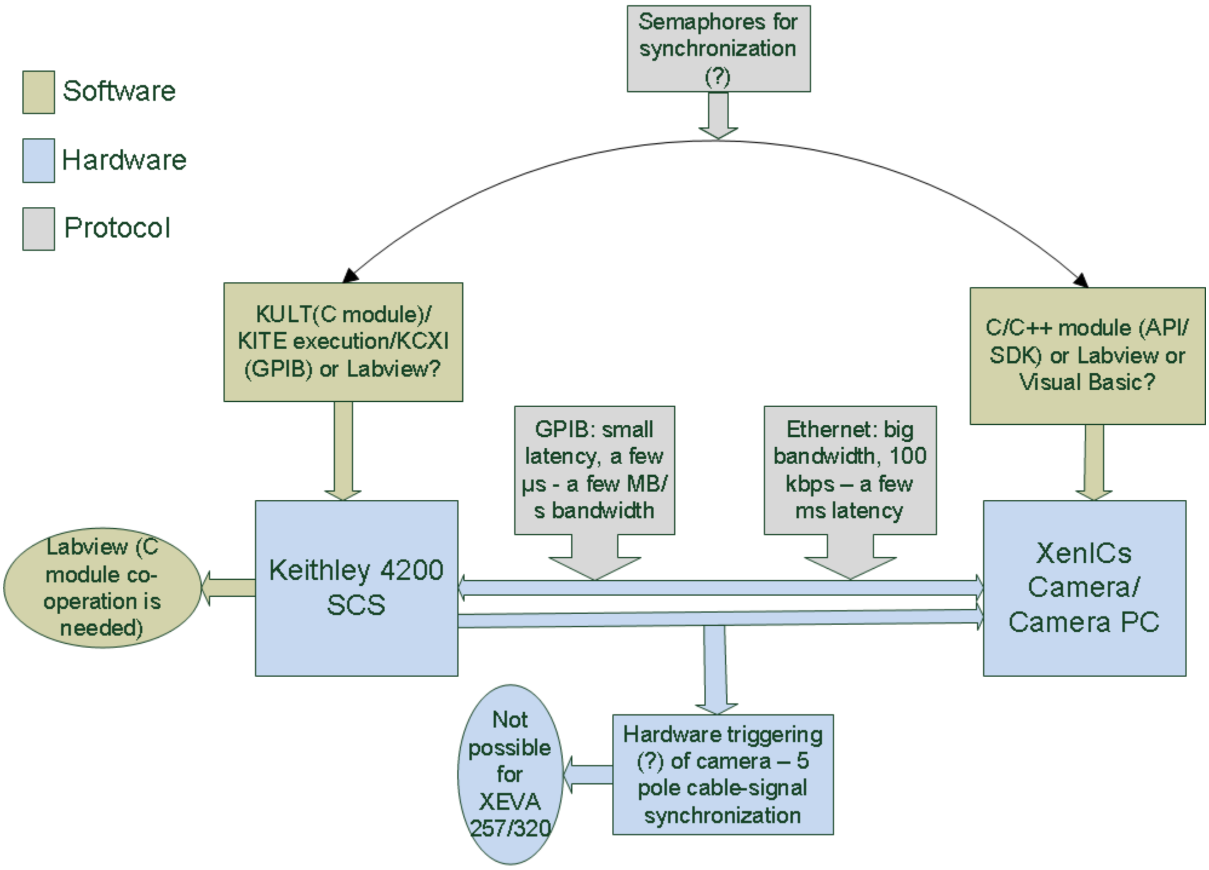

figure 1. Thinking process diagram.

The GPIB (General Purpose Interface Bus) was considered at the beginning of the design process as an option for communication between Keithley 4200 SCS and the camera (due to its small latency). Keithley has a GPIB port and it can receive commands remotely. The camera does not have a GPIB port and cannot respond to remote GPIB commands directly. Keithley 4200 SCS could receive commands remotely from the computer where the camera is connected. A GPIB port is available on this computer. Ethernet was also considered as a protocol for remote control of camera/Keithley 4200 SCS. It has higher latency than GPIB. Its high bandwidth makes it more proper for data transfer. Unfortunately, the GPIB/ethernet connection between two computers was left because of two reasons. Mainly, it was not possible to combine remote control of Keithley 4200 SCS with XCamera API and properly synchronize them. Moreover, GPIB commands are not as functional as C modules which are executed locally in Keithley 4200 SCS and have full control on its internal instruments. Another possibility for communication between Keithley 4200 SCS and the camera was to use hardware triggering. Unfortunately, a five-pole hardware triggering port is not available to the models of cameras that exist in the lab of the SC (Semiconductor Components) group. This port exists for newer models of Xenics cameras. The former complications led to the second plan where Keithley 4200 SCS and the camera are connected with a USB cable and their synchronization is implemented through semaphores. The software and hardware details of the latter setup configuration will be described next.

2.1 Software

C and C++ are the programming languages which were used for the implementation of the software. Two modules are written in C and C++: one is for the electrical characterization machine (C - Keithley 4200 SCS) and the other one is for the camera (C++ - XEVA 257/XEVA 320). The internal modules of Keithley 4200 SCS are written in C. Two types of C modules exist in Keithley: the interactive test modules (ITMs) and the user defined test modules (UTMs). ITMs offer an interactive graphic interface. ITMs are provided by the manufacturer of the equipment. On the other hand, UTMs offer less graphics performance but more programming flexibility. UTMs are modules which can be created by the user. Therefore our efforts were focused on UTMs. C++ or C (C++ and C functions exist for the camera control) is a possibility for the camera though its SDK (Software Development Kit). Many functions exist in this API (application programming interface) which can adjust many parameters of the camera such as its integration time. C++ is preferred for the camera process because it is practically found that C functions do not have proper control on the camera. Semaphores are used for the interprocess synchronization. These two processes and their interprocess communication with semaphores constitute a software tool. This tool is used for the implementation of the synchronized electrical and optical measurements.

Labview drivers exist for both Keithley 4200 SCS and camera. Labview is not preferred because it limits the functionality of Keithley 4200 SCS. Co-operation of C module with Labview is needed in order to fully control the internal instruments. To maintain uniformity to the system, Labview is also excluded for the camera and C++ is preferred instead.

2.1.1 Semaphores

Semaphores are a variable type introduced by Dijkstra at 1965 **[5].** Semaphores are ruled by two "atomistic" actions of "wait" and "release" **[6], [7].** Wait decrements the value of semaphore when its value is positive while release increments its value. The semaphore is blocked when its value is equal to zero or even negative. An example of synchronization between two processes is **[6]:** having two processes P_1 and P_2 with statements S_1 and S_2 and setting a rule that P_2 should run after P_1. This is how a "synch" semaphore is used to synchronize P_1 and P_2:

Process P_1		***Process P_2***
S_1;		Wait(synch);
Release(synch);	**and**	S_2;

2.1.2 Programming interfaces

Programming interfaces play a major role in the creation of the software. The way the interfaces co-operate in the software developed within this project is shown at figure 2:

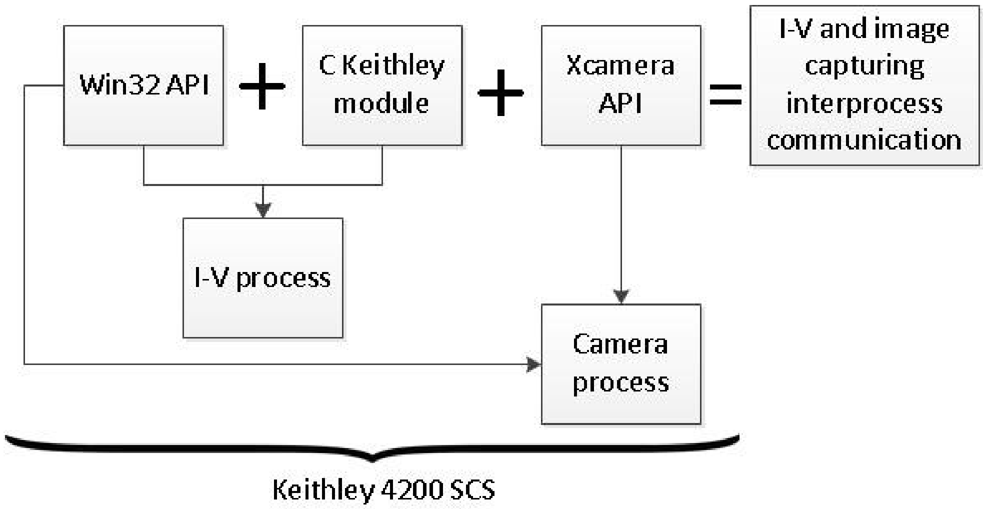

figure 2. Programming interface of Win32, XCamera and C Keithley module co-operation.

The win32 API commands in combination with a C Keithley module constitute the I-V process which captures the electrical data. The combination of win32 and XCamera API commands constitute the camera process which captures the images. Both processes run on Keithley 4200 SCS where the camera is connected to with USB. These two processes are synchronized with semaphores. This is how the structure of each process loop looks like (figure 3):

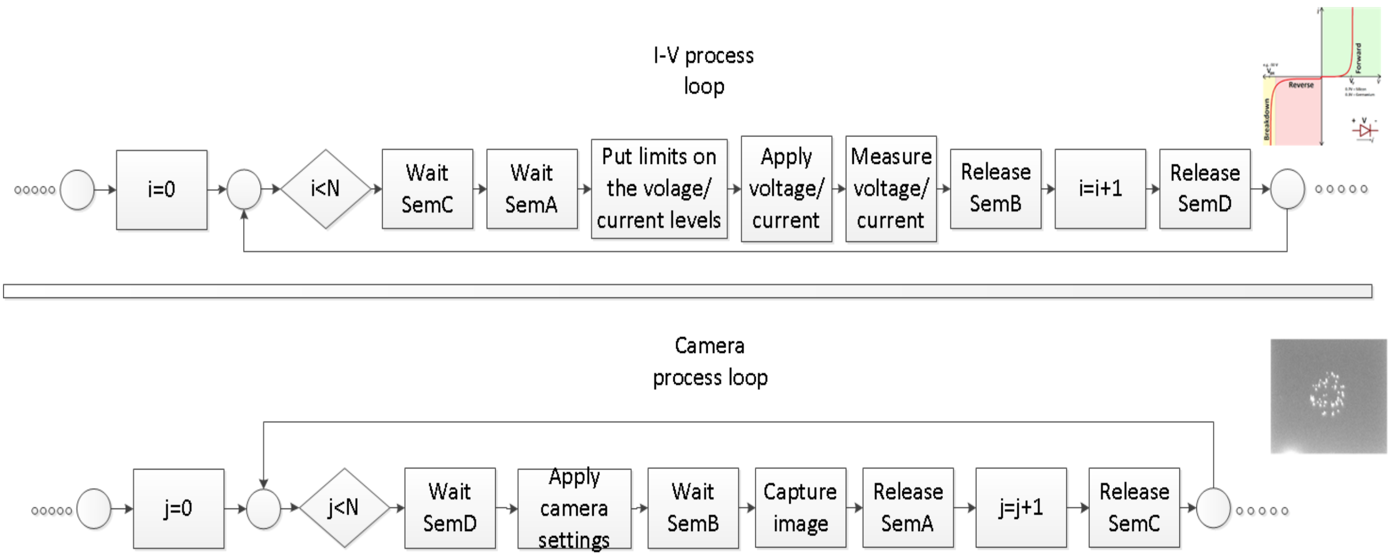

figure 3. Loop structure for I-V (Keithley 4200 SCS) and camera process.

From figure 3, it can be seen that the I-V process loop consists of a command set which includes three basic instructions: put compliance to voltage/current levels applied, apply voltage/current on the device and measure voltage/current from it. The second loop, the so-called camera loop, contains the application of the camera settings and the capturing of image by the camera.

In this configuration, four semaphores are used for the synchronization of the processes. Two semaphores synchronize the loops and two the I-V with image capturing part. This is how the synchronization of processes is implemented. The initial configuration included two semaphores. This number of semaphores was found insufficient to properly synchronize the two processes. The reason is that the camera loop contains the application of the camera settings which is a time consuming process and it is accompanied by the image capturing process. The latter process is the part of the code which needs to be synchronized with the I-V part of the Keithley 4200 SCS.

For further details on the code written for these two processes please visit Appendix A.

2.1.3 Software suite

The software suite of Keithley 4200 SCS consists of KITE (Keithley Interactive Test Environment), KULT (Keithley User Library Tool), KCON (Keithley CONfiguration) and KXCI (Keithley External Control Interface). KITE is the suite for module execution, KULT (C compiler) is the suite which offers the possibility to user to create his own modules, KCON is the tool for the configuration of the equipment and KXCI is the control interface which permits GPIB communication.

The software suite of the camera is the X-Control GUI where the integration time and other parameters relevant to the capture of the image can be adjusted. The X-Control version used within this project is designed for Windows XP (32 bit). Keithley is a Windows 7 machine. This compatibility issue was solved with hardware virtualization through Windows XP mode feature **[8].** X-Control GUI is necessary for inspection of the sample and correct alignment of the camera.

2.2 Hardware

The setup mainly consists of two instruments, an electrical characterization machine: Keithley 4200 SCS and a camera: InGaAs XEVA 257/320. The camera is connected to Keithley 4200 SCS via a USB cable (four USB ports available). Other instruments used are the probe station, the microscope and the cooling unit of the cameras. Next a short description of Keithley 4200 SCS and the cameras is given.

2.2.1 Keithley 4200 SCS

Keithley 4200 SCS is an instrument which offers the possibility of I-V (continuous or pulsed) and C-V measurements. The Keithley 4200 SCS used within this assignment consists of four SMUs (Stimulus Measurement Units) and one CVU (Capacitance Voltage Unit). Keithley 4200 SCS can act as a Windows 7 computer as well. The reference manual of Keithley 4200 SCS offers a more complete picture of the entire hardware system **[9]**. Keithley 4200 SCS is connected to the probe station which is the bridge between the sample and the setup. This probe station is a Karl Suss PM8.

2.2.2 Xenics cameras

The Xenics XEVA-257 and XEVA-320 InGaAs cameras are two CCD (Charged Coupled Devices) camera models developed especially for the laboratory of semiconductor components of UT (University of Twente) by Xenics. The USB cameras are equipped with a thermoelectrically cooled detector (Peltier element). The manual of the camera can provide further information on the hardware of the camera **[10]**. A Mitutoyo WF microscope (similar to FS70) was used for inspection of the samples during the measurements. A magnification of 50 times is used for the capture of images. The numerical aperture of this lens is 0.42 **[11]**. The diffraction limit (resolution) is $\lambda/2N_A$. The wavelength of our interest is in the range of 580 to 620 nm **[16]**. Therefore the resolution is 714 nm (for a wavelength of 600nm). Moreover, the cooling unit of the cameras is a TEK – TEMP RK-19.

2.3 Setup structure

The initial design of the setup included two computers: Keithley 4200 SCS and camera PC connected to each other through GPIB or Ethernet. This form of the setup is depicted at figure 4:

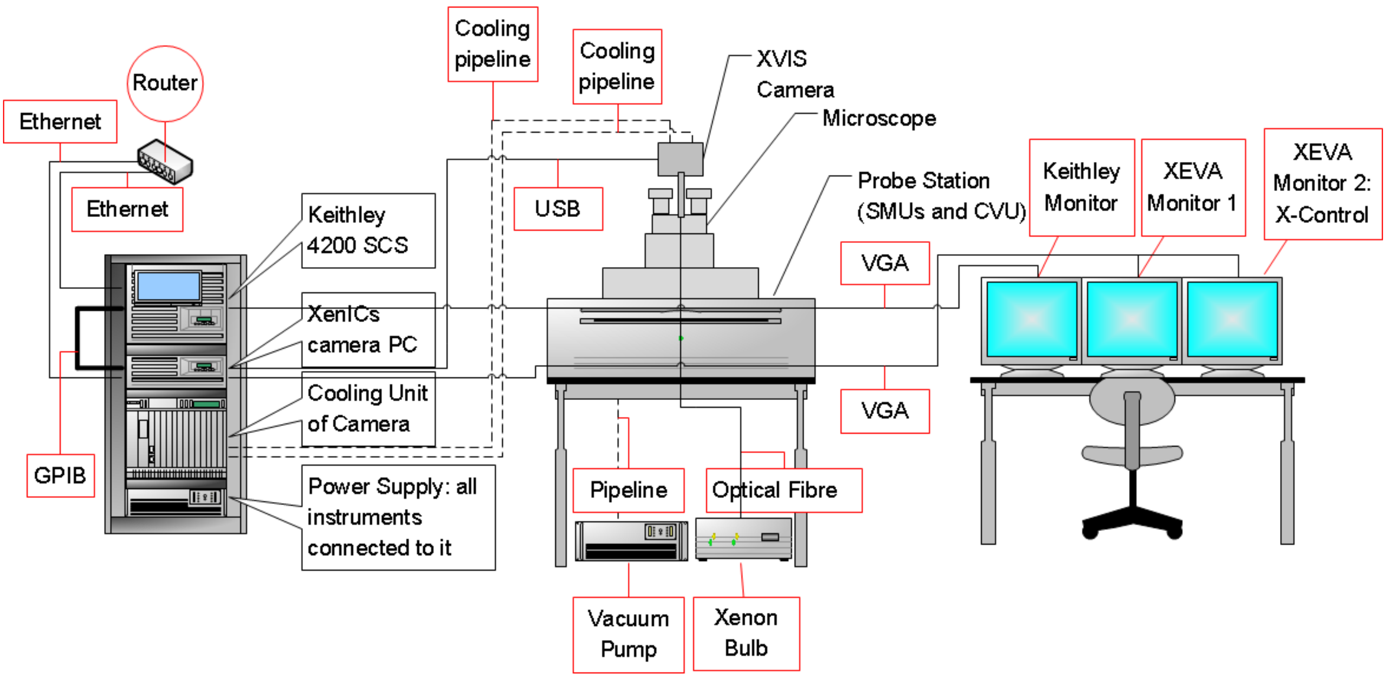

figure 4. The structure of the setup according to the initial plan.

The setup depicted at figure 4 was not used due to software and communication issues between Keithley 4200 SCS and the camera. Specifically, it was not possible to combine the remote GPIB control of Keithley 4200 SCS (KCXI) with X-Control API of the camera for the automation of the measurement. On the other hand, the GPIB port is not directly mounted on the camera but on the camera PC instead. The camera only includes a USB cable. This is the reason a simpler setup, depicted at figure 5, is used instead where Keithley 4200 SCS and Xenics camera are connected with a USB cable. This version of the setup is shown at figure 5:

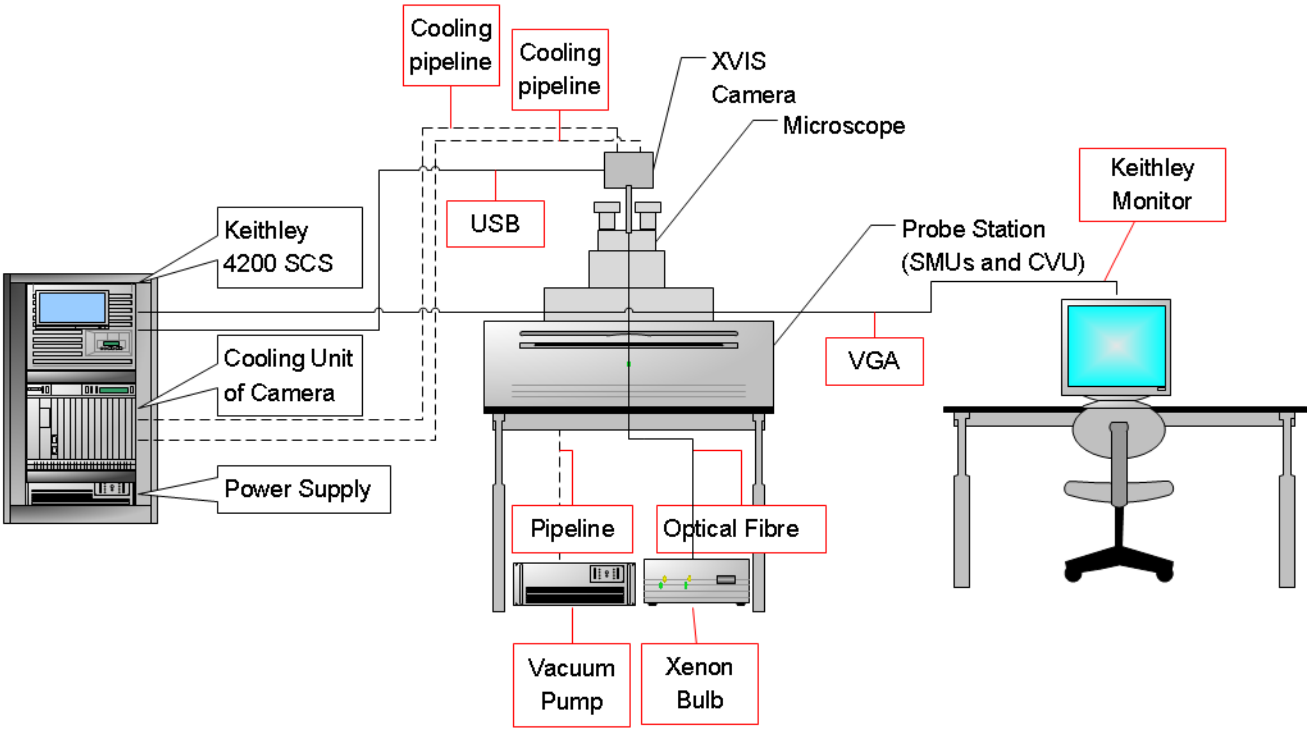

figure 5. A schematic of the setup according to the 2nd plan.

As it can be seen at the top left part of figure 5, there is a cabinet which contains Keithley 4200 SCS, the cooling unit of camera and the power supply. Both Keithley 4200 SCS and cooling unit are connected to the power supply located at the bottom of the cabinet. The cooling unit exists for the temperature control of the camera. The camera is directly connected to Keithley 4200 SCS via a USB cable. Next to the cabinet, the probe station is located where the camera and microscope are set at the top of it. The light comes from a xenon bulb under the probe station. Moreover, the Keithley 4200 SCS is connected to a VGA monitor.

Next, a brief description on a few properties of the material of our interest, Silicon, follows.

3. Silicon Properties

Silicon (Si) has an indirect bandgap of 1.12 eV at 300K **[12]**. Its bandgap is indirect as opposed to the majority of the light-emitting semiconductors where their bandgap is direct e.g. AlGaAs **[13]**. The figure 1 shows the energy dispersion of Si and its indirect bandgap. The minimum of the conduction band and the maximum of the valence band occur at different wavenumbers:

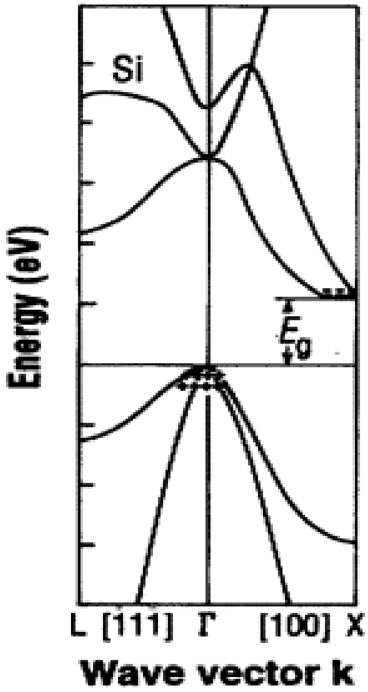

figure 6. Energy dispersion of Si. The minimum of conduction band and the maximum of valence band occur at different wavenumber **[13]**.

In semiconductors with a direct bandgap, radiative transitions occur spontaneously since an electron excited from the conduction band can fall to the valence band without undergoing a change in the momentum. Materials with indirect bandgap have radiative transitions with one extra condition: change in the momentum. This is the reason why light from materials with indirect bandgap such as Si, is emitted at a low quantum efficiency.

Regarding the optical behavior of Si, its indirect bandgap causes the emission of infra-red light **[15]**. However, it emits visible light when it is put in the avalanche state **[17]**, **[18].** A part of this light (its energy) exceeds the bandgap energy of Si. This light generated comes from direct and phonon-assisted transitions. Emission pattern appears as a group of localized spots (microplasmas). These spots are found to be correlated with internal crystal imperfections (defects) **[19]**. Light generated due to defects in Si are reported in several cases **[20]**, **[21]**, **[22]**, **[23]**, **[24]**.

Furthermore, the attenuation length of Si for a wavelength range from 250 to 1450 nm is shown in figure 7:

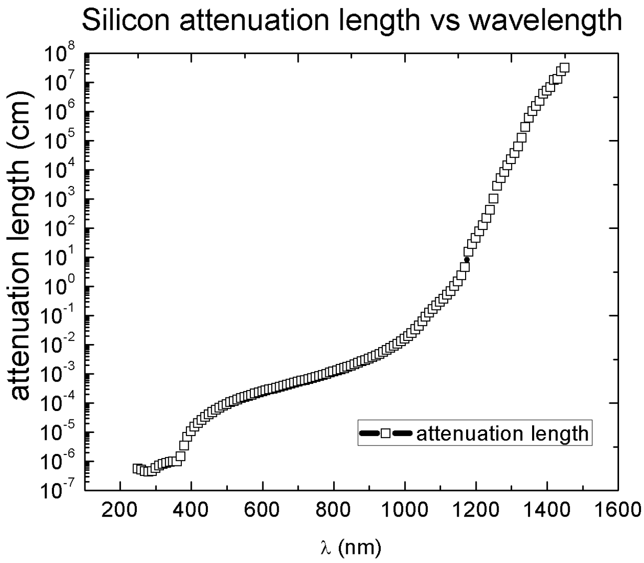

figure 7. Attenuation length of Si in log-scale **[14]**.

In the next chapter, the structure of the avalanche Si diodes measured within this project is described.

4. Diode structure

The diodes measured during the experiments conducted are basically ultra-shallow Silicon (Si) p-n diodes **[3]**. They emit visible light in the avalanche mode and infrared light when they are biased in forward mode. More details on the device structure and the phenomena behind the visible light emission are analyzed next.

4.1 Avalanche mode

Although silicon is not preferred as a light source, avalanche mode Si light emitting diodes emit light in the visible range where high speed intensity modulation is feasible (~20 GHz) **[16]**. Avalanche mode diodes are based on the phenomenon of electron avalanche which occurs due to impact ionization. Impact ionization is the collision of carriers with Si lattice. This collision causes carrier multiplication and is dependent on the max. field of the space-charge region. This field increases as the reverse bias increases and generate more electron-hole pairs. Secondary carriers generate electron-hole pairs after a certain critical field value. This generation triggers a domino effect and the current increases by several orders of magnitude. This is the so-called avalanche multiplication.

4.2 Ultra-shallow UV-sensitive PureB p+-n junctions

The diodes used within this report are fabricated in Si with PureB technology where pure Boron is formed with Chemical Vapor Deposition (CVD) [3]. Diodes fabricated with this methodology show remarkable internal/external quantum efficiency, dark current and responsivity degradation. CVD creates PureB layer such that bare-2 nm Boron layers are used as front entrance windows. Boron layers can be also used as a p^+ layer and form a p^+n junction. Fabrication details and diode cross-sections will follow next.

Next, some information on the fabrication of the ultra-shallow PureB p^+-n junctions follows.

4.2.1 Device Under Test (DUT) fabrication

The flow diagram depicted at figure 8 [3] describes the flow of the PureB ultra-shallow p^+-n junction fabrication:

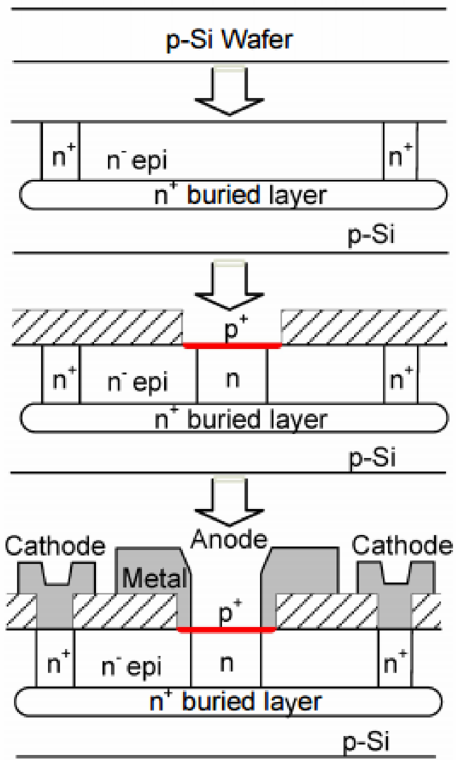

figure 8. Process flow of DUT **[3]**.

As it can be seen in figure 8, the fabrication [3] starts with a p-type (100) 2-5 Ωcm Si substrate. Then a n- epitaxial layer is formed on a n^+ buried layer. The latter layer is linked to n^+ plugs. The active area of the detector is developed with a n-enrichment implantation through a 30-nm thermal silicon oxide layer. A 300 nm-thick TEOS layer is deposited next by LPCVD. Annealing of implants is then performed at 950 °C for 20 min in argon gas. Plasma etching of the oxide layer is conducted in order to open the anode contact windows to the Si. Native oxide is removed with HF 0.55% and the samples are dried with Marangoni method. PureB layer deposition is following from diborane in an ASM Epsilon 2000 reactor for 6min at 700 °C. This layer is driven in at 850 °C for 1 min which increases the boron doping of the Si, contributing to the robustness of the p$^+$ region formed at the PureB-Si interface. Aluminum layer deposition follows of 675 nm at 50 ^{o}C. Then the windows are formed with plasma etching. A 2nd layer of Al with 1% of Si is deposited at the same temperature. Metal patterning is conducted while the light windows are formed by plasma etching of Si until 100-200nm and removing of Al (HF 0.55% for 3-5 min). Temperature annealing is the last processing step to anneal the contact between the Al and the PureB layer.

4.2.2 DUT geometry

The comparative dimensions of anode p$^+$ region (diameter D1), entrance window and n-enrichment region (diameter D2 at a distance L from the anode) are shown at figure 9 [3]:

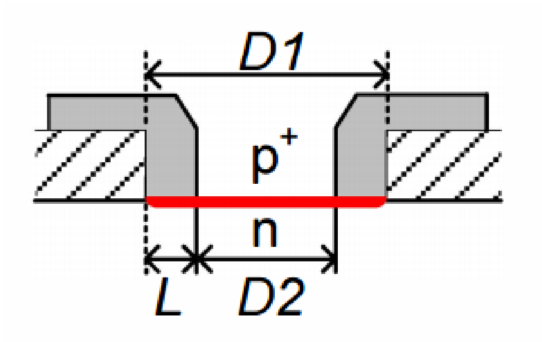

figure 9. DUT geometry **[3]**.

The cross-section and top image of the diode are better shown at figure 10:

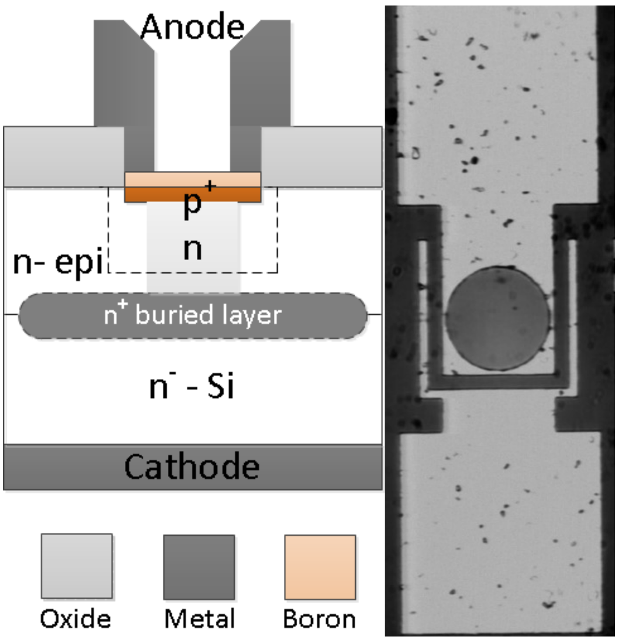

figure 10. At the left: the diode cross-section (V_{BR}=-7 V) while at the right: diode top image.

Furthermore devices with and without a n^+ buried layer are fabricated. The absence of the n^+ buried layer increases the effective doping level in the enrichment region and the breakdown voltage is decreased from 14 V to 7 V **[16]**. The n-enhancement implantation exists to control where the breakdown is occurring. Thus two sorts of diodes are measured regarding the break-down voltage within this project: 14 V and 7 V breakdown diodes. Regarding the geometry, circular and rectangular diodes are measured within the experiments conducted.

4.2.3 DUT doping

The doping profile obtained from simulations (approaching the real doping in the diode) is **[3]**:

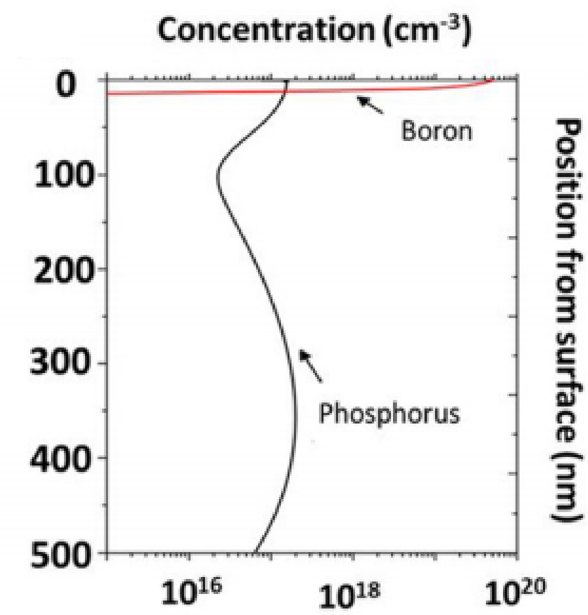

figure 11. Doping profile of DUT.

Next, information on the spectral response of diodes follows.

4.3 Electroluminescent spectra of DUT in avalanche mode

An opto-electronic model which describes the output spectrum of an avalanche Si p^+n light emitting diode as a function of bias have been suggested **[16]** earlier. The spectral response of both diodes with breakdown voltage of 7 V and 14 V has been measured at certain biases. The experimental data retrieved were compared with the model developed to confirm its validity (figure 12):

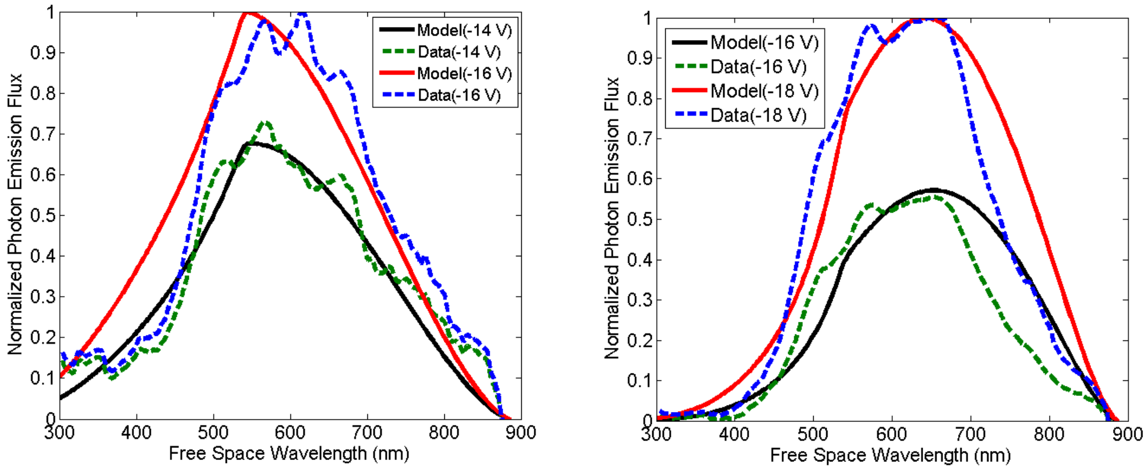

figure 12. Spectral response of avalanche diodes with breakdown voltage of 7 V (left) and 14 V (right) respectively **[16]**.

The spectral irradiance in both 7 V and 14 V diodes is found to be peaking within ~580-620 nm.

Next, a short description of the electro-luminescence in DUT at avalanche mode follows.

4.4 Electro-luminescence in DUT at avalanche mode

Visible light is emitted from a p-n Si junction when this is biased in the avalanche mode **[1]**, **[2]**, **[17]**, **[18]**, **[19]**, **[20]**, **[23]**, **[24]**, **[25]**, **[28]**, **[29]**, **[30]**, **[31]**, **[32]**. This visible radiation is expressed as scattered spots along the active area of the diode as it has been observed in several cases in literature (Figure 13):

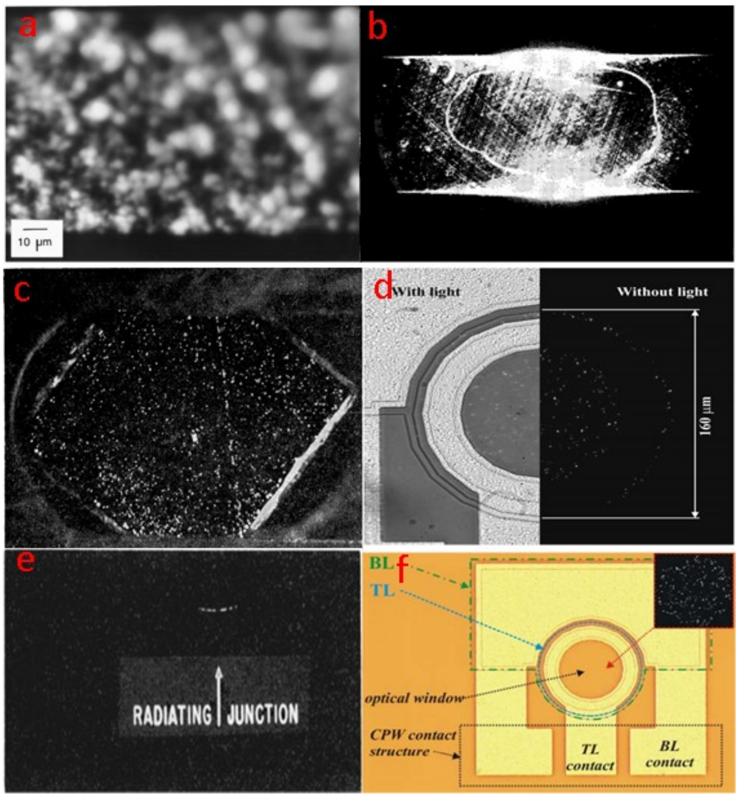

Figure 13. Visible light spots emitted under avalanche mode in several silicon junctions reported in literature (a **[25]**, b **[19]**, c **[28]**, d **[2]**, e **[1]**, f **[20]**).

Light spots appearing along the active area of the DUT in the avalanche mode are shown at figure 14:

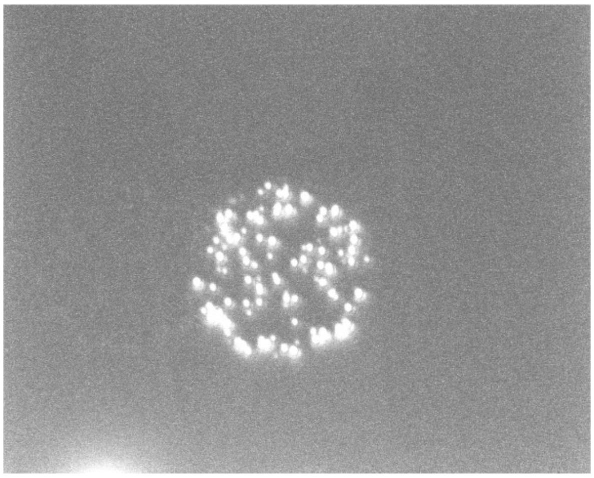

figure 14. Light spots appearing along the active area of the DUT in the avalanche mode.

The light spots shown at figure 14 are often called microplasma spots **[17]**, **[19]**, **[23]**, **[28]**, **[32]**. The breakdown is considered to be an equivalent of gas plasma discharge, the microplasma **[33]**. This is the reason the term microplasma is used here in a solid state physics analysis. These spots are often correlated to dislocations (crystal abnormalities) in the material (Si) **[25]**, **[19]**, **[23]**, **[18]**, **[28]**, **[24]**, **[30]**, **[2]**. Here in this report, the term “defects” will be used covering a range of possibilities for the cause of the radiation such as: structural lattice imperfections and non-uniformity in doping. Generally, the light is generated into areas of the diode where the electrical field is strongest.

Next, a description of the conditions of the experiments conducted within this project follows.

5. Experiment description

Overall, three sorts of experiments were conducted within this project. The first experiment was to check the spatial variance of spots when the diode was repeatedly biased in the avalanche mode (ON) with intermediate low reverse bias states (OFF). The second one was to check the intensity and number of spots due to increase of the bias. The last one was for the comparison of the intensity of light (number of photons) coming out from a visible and infrared emission for the same DC electrical input power.

The figure 15 describes the arrangement of the instruments used during these experiments:

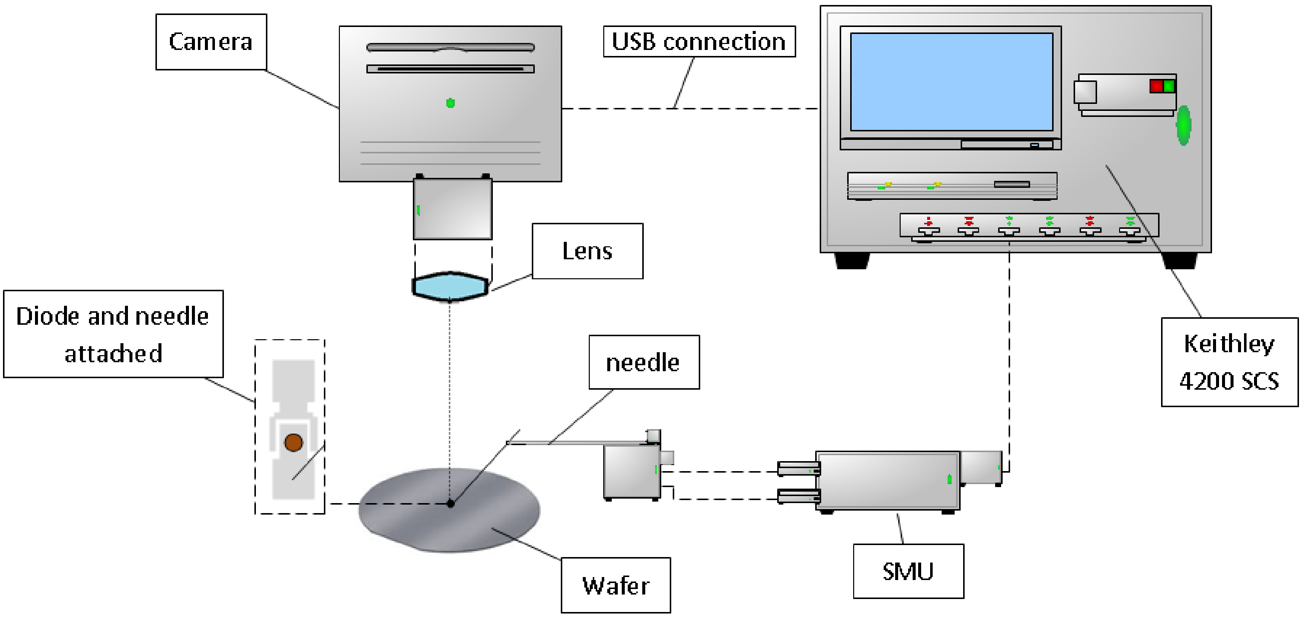

figure 15. Arrangement of instruments for the implementation of the electro-optical measurement.

As it can be seen from figure 15, the setup of the measurement consists of a camera, a magnifying lens (50 times magnification in all experiments), Keithley 4200 SCS, the internal SMU (Stimulating Measurement Unit) and a probe. The lens is properly aligned with respect to the camera such that magnifying is achieved. The probe (needle) is attached to the anode of the diode and connected to the SMU. SMU is an internal measurement instrument of Keithley 4200 SCS (it contains 4 SMUs and 1 CVU in total).

5.1 Experiment #1: spatial variance of spots in repeated cycles of avalanche-mode

After a brief explanation of the measurement experimental setup, the first experiment which checks the spatial variance of the spots when the diode is put in avalanche mode for multiple cycles is demonstrated at figure 16:

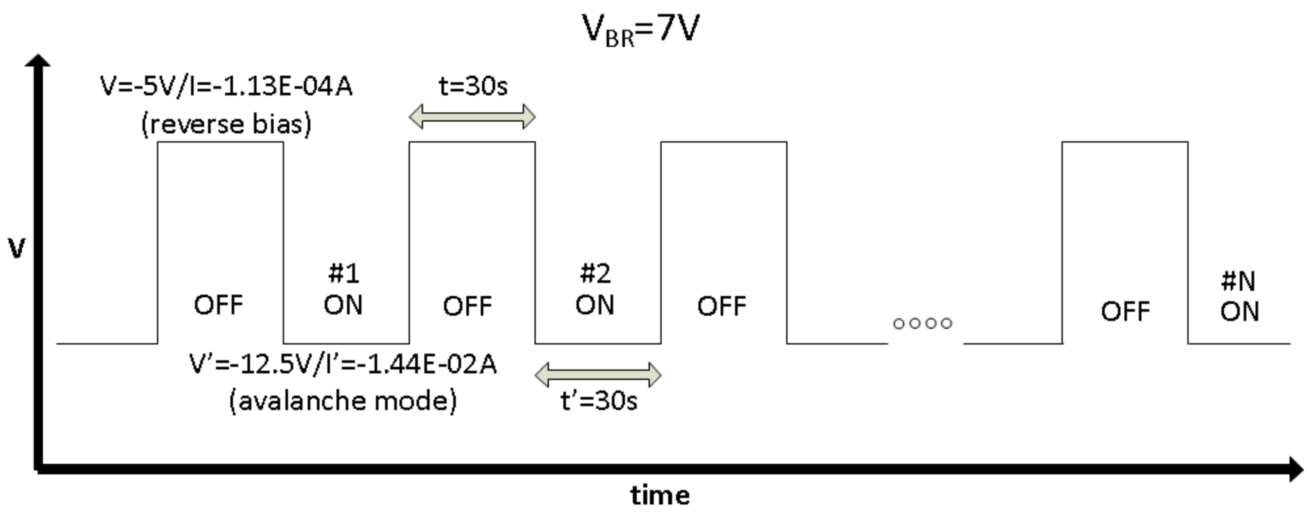

figure 16. Bias and time arrangement for experiment #1.

In this experiment, repeated cycles of avalanche mode biasing (ON) and low (weak) reverse bias states (OFF) are applied. The conditions of this experiment are that the avalanche mode is at -12.5V (-1.44E-02A) while the weak reverse (OFF) bias state at -5V (-1.13E-04A). The integration time of the camera which determines the execution time and capture images only in this state is 30s. The time duration of the so-called off state (weak reverse bias) where no image is taken is also 30s.

5.2 Experiment #2: intensity variation due to stepped bias increase

The 2nd experiment is a stepped (incremented) bias measurement where each bias step is equal to -1 V and the integration time of the camera in each step is equal to 30s (figure 17):

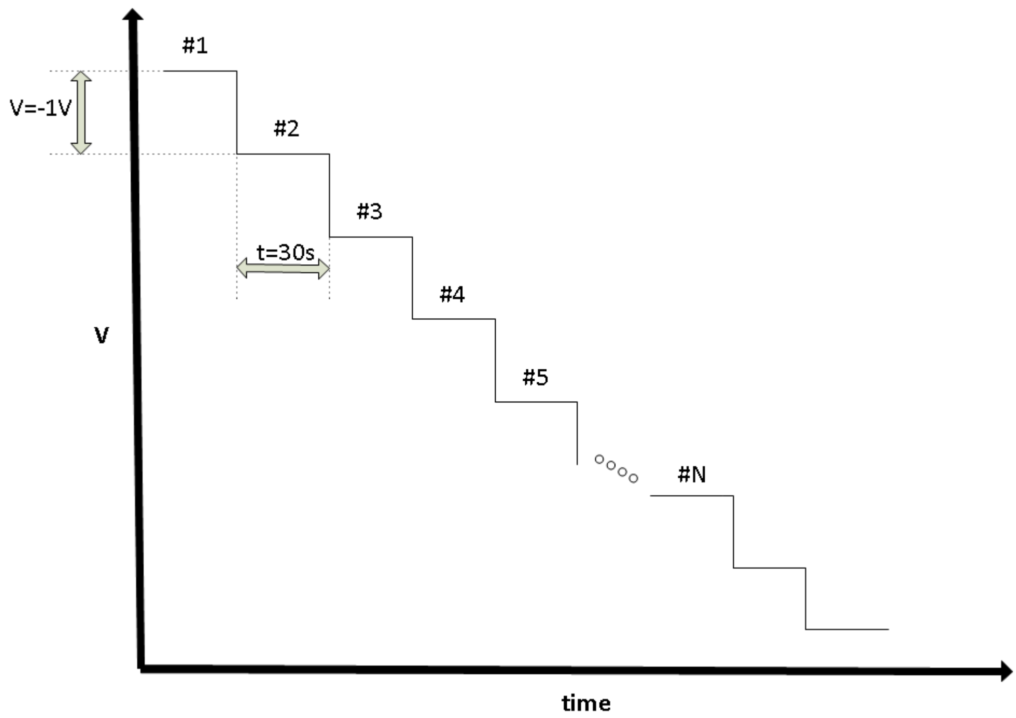

figure 17. Incremental bias experiment with its bias and time arrangement. V is for voltage in y-axis and time in the x-axis.

The goal of this experiment is to show the variation of the light intensity according to the stepped bias increase.

This measurement is repeated for multiple cycles.

5.3 Experiment #3: visible and infrared (IR) emission of DUT

The 3rd kind of measurement includes the discussion between a visible and an infrared (forward bias) emission under the same DC electrical input power. The power supply selected for this experiment is 0.18W. The forward bias is at 5 V (3.61E-02 A) while the reverse bias at -12.5 V (-1.44E-02 A).

6. Experimental results

The main aim of the experimental work done within this project was to investigate the optical response of the avalanche Si diode mainly under reverse bias in the avalanche mode. This general research question includes a group of sub-questions which will be answered within this report. The first research question is if there is a spatial variance in the light spots when the diode is repeatedly biased in avalanche mode and therefore to investigate if fixed defects are the cause of the visible light spots. The results indicate that the same intensity and arrangement of spots are occurring for the multiple cycles of the measurement. Thus the same fixed defects cause the emission of light in avalanche mode. The second question is if we get increased intensity and number of spots for increased bias. The experimental results indicate increasing intensity and number of spots for increasing bias indeed. The next research question is if the size of the diode affects the intensity and the number of emerging spots in the diode. The results indicate increasing number of spots. The mean intensity decreases for increasing diameter (for a fixed bias). Another research question is the discussion of visible and infrared light intensity (number of photons) for the same power supply. The result is that the infrared radiation appears as a ring of light around the perimeter of the diode. Another comparison attempted is the comparison between the two kinds of diodes that exist in the wafer: diodes with 7 V and 14 V breakdown voltages. The results indicate that the 14 V diodes do not show localized light spots but a glow around the diode perimeter during the avalanche mode. More spatially uniform light is emitted during the forward bias (infrared emission) for this type of diode.

6.1 Visible emission experiments in avalanche mode

Emission experiments have been conducted in order to demonstrate the operation of the setup. Specifically, in one of experiments a diode was forced to enter avalanche mode multiple times. Reverse bias lower than the breakdown voltage is applied in the mean time between two subsequent avalanche states. The biasing lasts equal time as the integration time of the camera. This experiment for six iterations provides six visible emissions as depicted at figure 18**:**

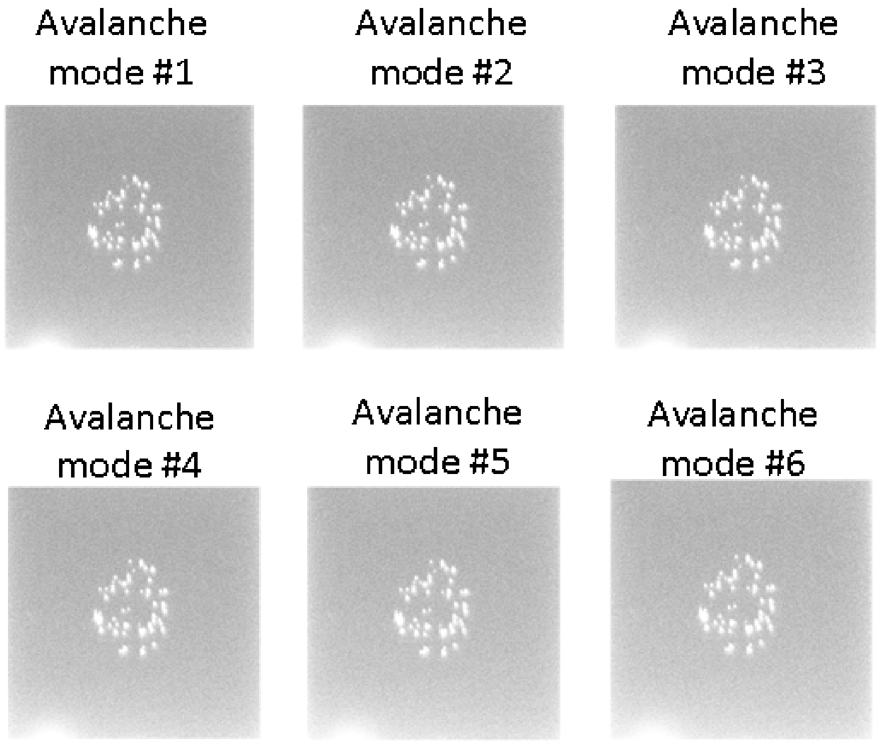

figure 18. Avalanche mode: six visible emissions for six iterations.

The six visible emissions show the same spatio-temporal invariance of spots. This can be mathematically shown in terms of correlation coefficient. The correlation coefficient of visible emissions is approximately one which means that the arrangement of spots remains the same from iteration to iteration.

The experiment conducted refers to a diode with a diameter of 40 µm and 1.5 µm anode ring lateral width. The experiment is repeated for diodes with diameters of 35, 30 and 27 µm which show the same behavior as noticed in the case of 40µm. Different anode ring sizes were tried of 1.5, 1 and 0.5 µm. All of them show same arrangement of spots in multiple avalanche states (correlation approximately 1). The Table 1 contains the correlation coefficients for all the sizes of the diodes measured:

Table 1. Table with correlation coefficients of all images taken for all diode sizes measured. d is for diameter and w for the lateral anode ring width.

number	d (um)	w (um)	correlation	number	d (um)	w (um)	correlation	number	d (um)	w (um)	correlation
1	40	1.5	0.9979	6	40	1	0.9962	11	40	0.5	0.9984
2	40	1.5	0.995	7	40	1	0.9947	12	40	0.5	0.9955
3	40	1.5	0.9906	8	40	1	0.9947	13	40	0.5	0.9911
4	40	1.5	0.9854	9	40	1	0.9909	14	40	0.5	0.9859
5	40	1.5	0.9826	10	40	1	0.9896	15	40	0.5	0.9878
number	**d (um)**	**w (um)**	**correlation**	**number**	**d (um)**	**w (um)**	**correlation**	**number**	**d (um)**	**w (um)**	**correlation**
16	35	1.5	0.9972	21	35	1	0.9986	26	35	0.5	0.9986
17	35	1.5	0.9971	22	35	1	0.9949	27	35	0.5	0.9957
18	35	1.5	0.9981	23	35	1	0.9932	28	35	0.5	0.9948
19	35	1.5	0.9955	24	35	1	0.9944	29	35	0.5	0.9952
20	35	1.5	0.9961	25	35	1	0.9957	30	35	0.5	0.9946
number	**d (um)**	**w (um)**	**correlation**	**number**	**d (um)**	**w (um)**	**correlation**	**number**	**d (um)**	**w (um)**	**correlation**
30	30	1.5	0.9987	35	30	1	0.998	40	30	0.5	0.9966
31	30	1.5	0.9968	36	30	1	0.9948	41	30	0.5	0.9921
32	30	1.5	0.9936	37	30	1	0.9901	42	30	0.5	0.986
33	30	1.5	0.9892	38	30	1	0.9844	43	30	0.5	0.9828
34	30	1.5	0.9853	39	30	1	0.9874	44	30	0.5	0.9916

The bias conditions for all the diodes measured in this experiment are shown at Table 2:

Table 2. Bias conditions for all the diodes measured during the experiment #1 (for both ON and OFF states).

d (um)	w (um)	$V_{(ON)}$ (V)	$I_{(ON)}$ (A)	$V'_{(OFF)}$ (V)	$I'_{(OFF)}$ (A)	$t_{(ON)}$ (s)	$t'_{(OFF)}$ (s)
40	1.5	-1.25E+01	-1.44E-02	-5.00E+00	-1.12E-04	3.00E+01	3.00E+01
40	1	-1.27E+01	-1.36E-02	-5.00E+00	-6.82E-05	3.00E+01	3.00E+01
40	0.5	-1.25E+01	-1.27E-02	-5.00E+00	-1.49E-04	3.00E+01	3.00E+01
35	1.5	-1.29E+01	-1.25E-02	-5.00E+00	-1.05E-05	3.00E+01	3.00E+01
35	1	-1.33E+01	-1.28E-02	-5.00E+00	-8.57E-06	3.00E+01	3.00E+01
35	0.5	-1.21E+01	-1.34E-02	-5.00E+00	-2.24E-03	3.00E+01	3.00E+01
30	1.5	-1.33E+01	-1.26E-02	-5.00E+00	-1.10E-04	3.00E+01	3.00E+01
30	1	-1.34E+01	-1.17E-02	-5.00E+00	-5.07E-05	3.00E+01	3.00E+01
30	0.5	-1.33E+01	-1.13E-02	-5.00E+00	-7.77E-05	3.00E+01	3.00E+01
27	1.5	-1.37E+01	-1.19E-02	-5.00E+00	-5.78E-06	3.00E+01	3.00E+01
27	1	-1.35E+01	-1.14E-02	-5.00E+00	-3.62E-05	3.00E+01	3.00E+01
27	0.5	-1.32E+01	-1.31E-02	-5.00E+00	-2.68E-03	3.00E+01	3.00E+01

It has also to be underlined that the intensity of light in the emissions is also the same from iteration to iteration.

6.2 Varying bias

More experiments with diodes in avalanche mode were conducted. This time the bias is varying and values higher than the breakdown voltage (avalanche mode) are attempted. The emission spots of the visible emission for varying emission are clearly shown in figure 19 (diode with a diameter of 40 μm and a lateral anode width of 1.5 μm):

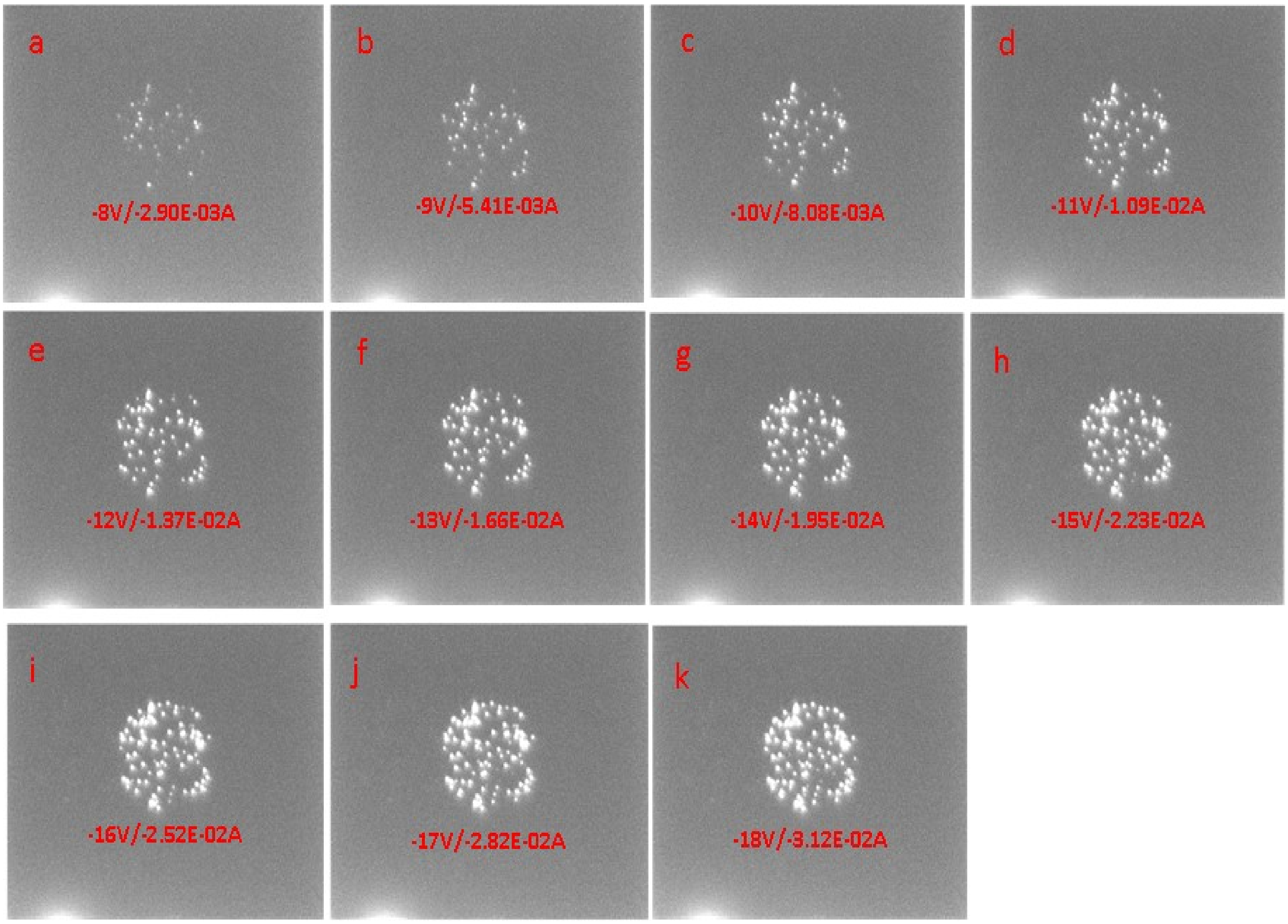

figure 19. Spots of visible light emissions from **a** to **k** for variable bias (-8 V to -18 V).

The appearance of visible light spots during the avalanche mode in Si p-n diodes is a well-known phenomenon in literature **[1], [2], [17], [18], [19].** The voltage varies from -8 to -18 V and more emission spots are generated (figure 19) as the bias increases. Specifically, the intensity and current generated with respect to bias is depicted at figure 20:

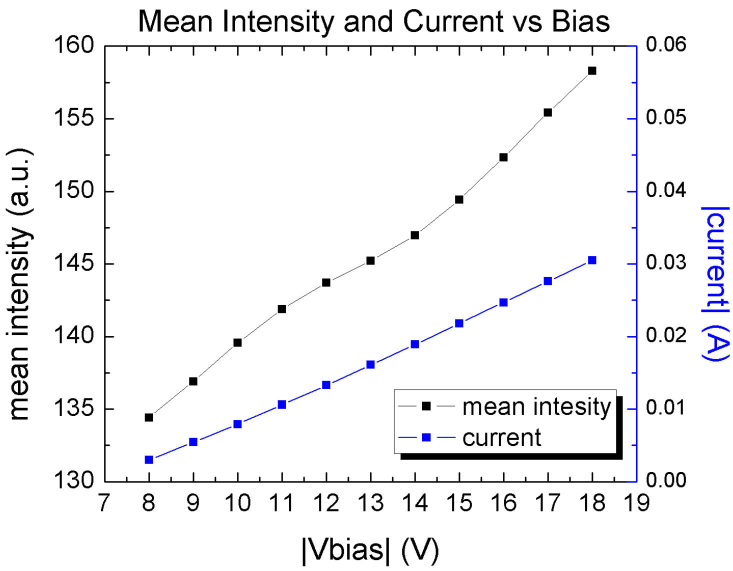

figure 20. Intensity in arbitrary units and current (absolute values) versus bias.

As it can be seen from figure 20, intensity (Appendix D) increases as bias increases (the current also increases) **[1]**, **[18]**. This is expected since more recombination takes place with increasing bias and more electron-hole pairs are generated and recombine in the microplasma areas **[32].** The number of spots is also changing with increasing bias. It specifically increases (figure 21) **[1]**, **[18]**:

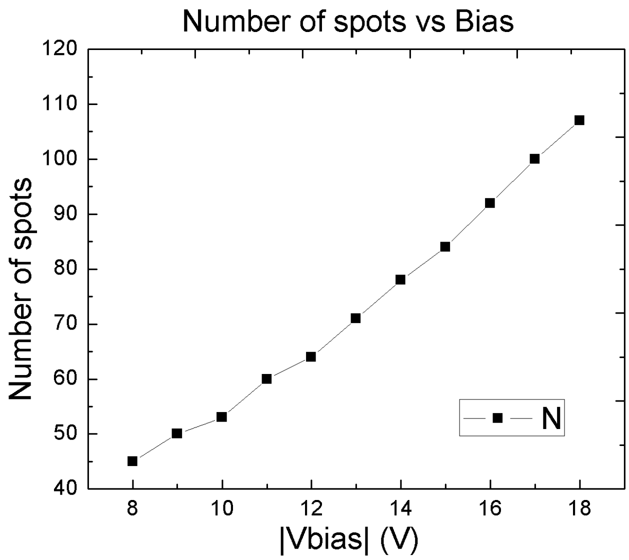

figure 21. Number of spots (N) versus bias.

The experiment of varying bias was repeated for diodes of 35 μm down to 1 μm. Ten devices of its sort were measured. The intensity (Appendix B) and current were averaged. The standard deviation is also calculated (Appendix B). This (figure 22) is a graph which compares the average intensity and current of a 40, 24, 12 and 3 μm diode:

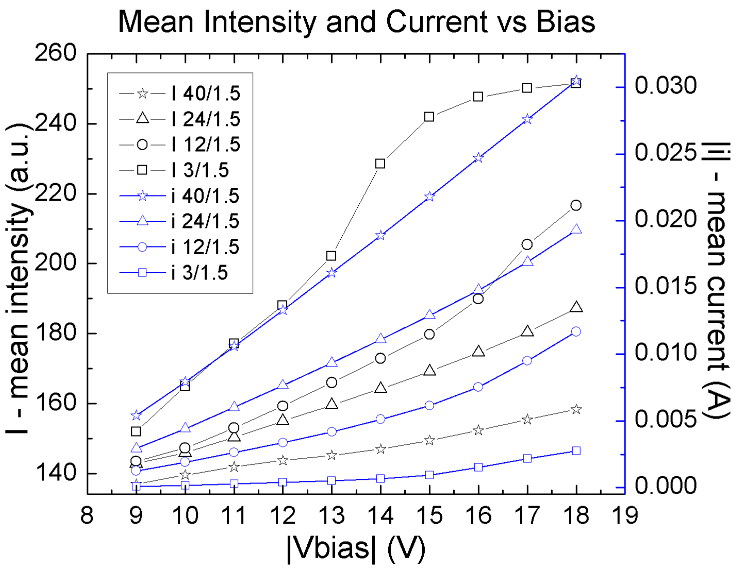

figure 22. Intensity (I) and current (i) generated for increasing bias for diodes of 40, 24, 12 and 3 μm (with an anode lateral width of 1.5 μm).

In figure 22, we can see bigger slope in the I-V for bigger size of diode. This is expected since the effective resistance decreases for bigger diameter. The standard deviation for current is negligible while the standard deviation for the intensity varies by 2% up to 7.5% in several cases (Appendix B). This is an indication for the non-uniformity of the wafer.

Indicatively, the breakdown for the diodes with diameter of 40, 24, 12 and 3 μm is shown at figure 23:

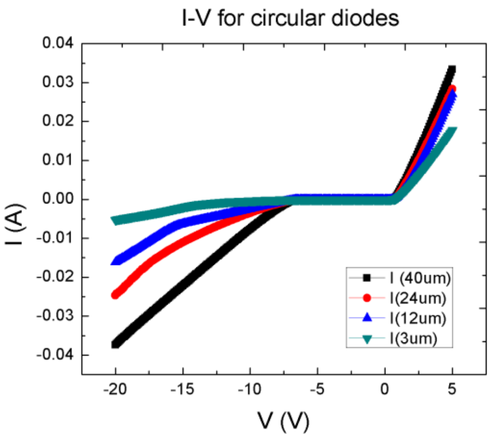

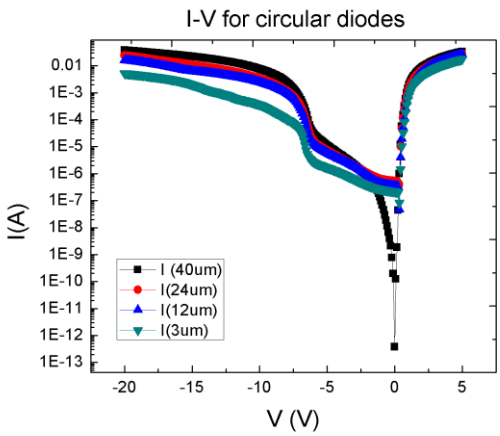

figure 23. I-V characteristics for diodes with diameters of 40, 24, 12 and 3 μm. Left: linear scale and right: log scale.

From figure 23, it can be seen that the breakdown occurs mostly at -7 V for all diodes while the slope decreases for smaller size of diode due to bigger effective resistance. The breakdown at -7 V is also shown at the I-V characteristic in log-scale.

The current density for the same diodes is shown in figure 24:

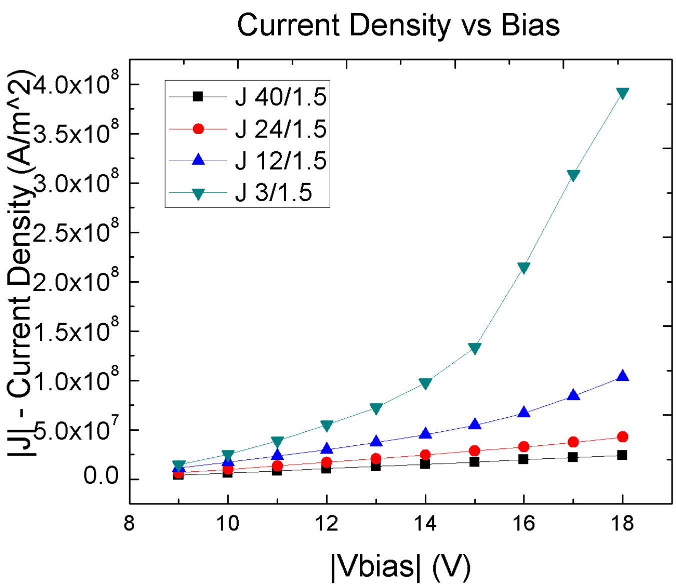

figure 24. Current density for diodes of 40, 24, 12 and 3 µm with a lateral anode width of 1.5 µm.

As it can be seen from figure 24, the current density is bigger for smaller diodes. This observation can lead us to the conclusion that the lateral resistance in the p-layer is playing a dominant role in determining the current.

Next, the intensity of central spots for diodes of different diameter is depicted:

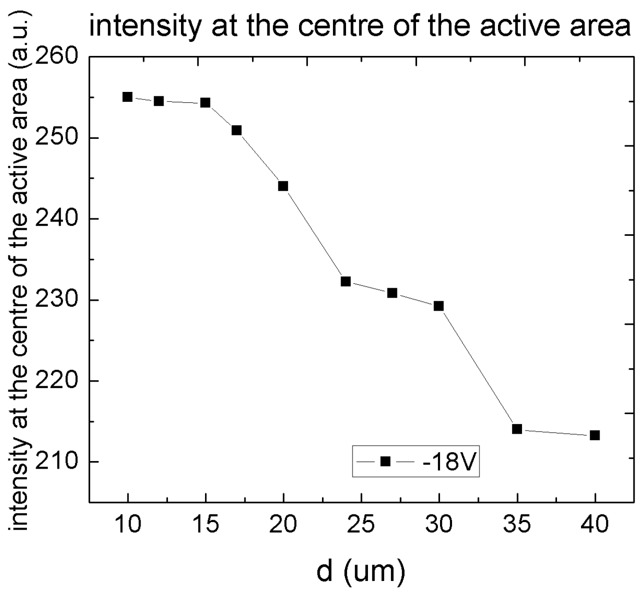

figure 25. Intensity of central spot for diodes from 40 µm down to 1 µm.

The intensity of spots close to the center of the active area increases with decreasing diameter. The electric field falls towards the center more for diodes with bigger diameter. This is a possible reason for why we see less intensity for bigger circular diodes. Another fact is that the curvature in small diodes is bigger and this causes higher electric field and consequently more radiation (intensity).

Interesting information we can obtain from the experimental results is the number of spots (Appendix G – technique of calculation) with respect to the size (perimeter/area, perimeter and area) of the diode (figure 26):

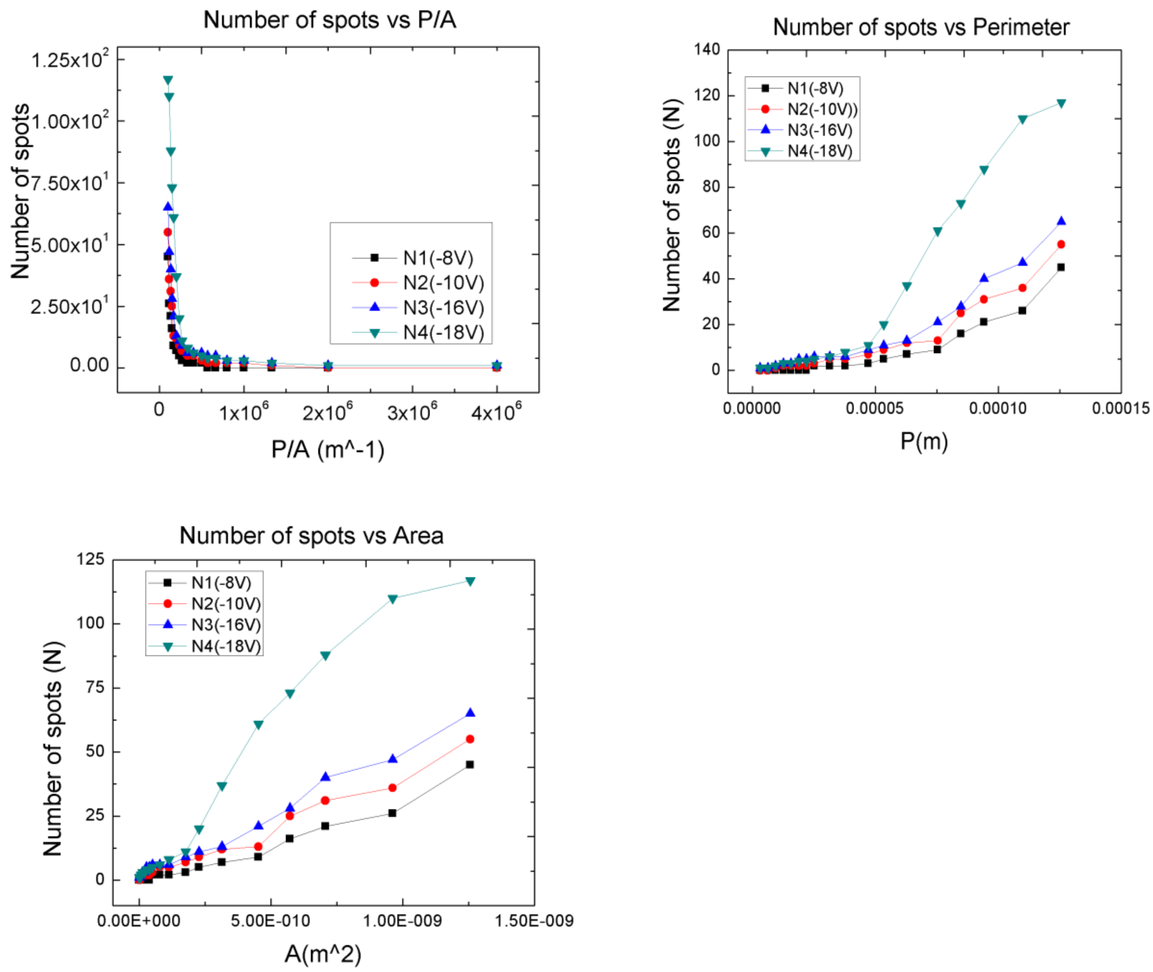

figure 26. Number of spots vs perimeter over area, perimeter and area for diodes from 40 to 1 µm for 4 selected biases.

From figure 26, specifically from the plots versus perimeter and area, it can be seen that the number of spots increase with respect to both area and perimeter (size of circular diode).

On the other hand, the density of spots (number of spots/area) is:

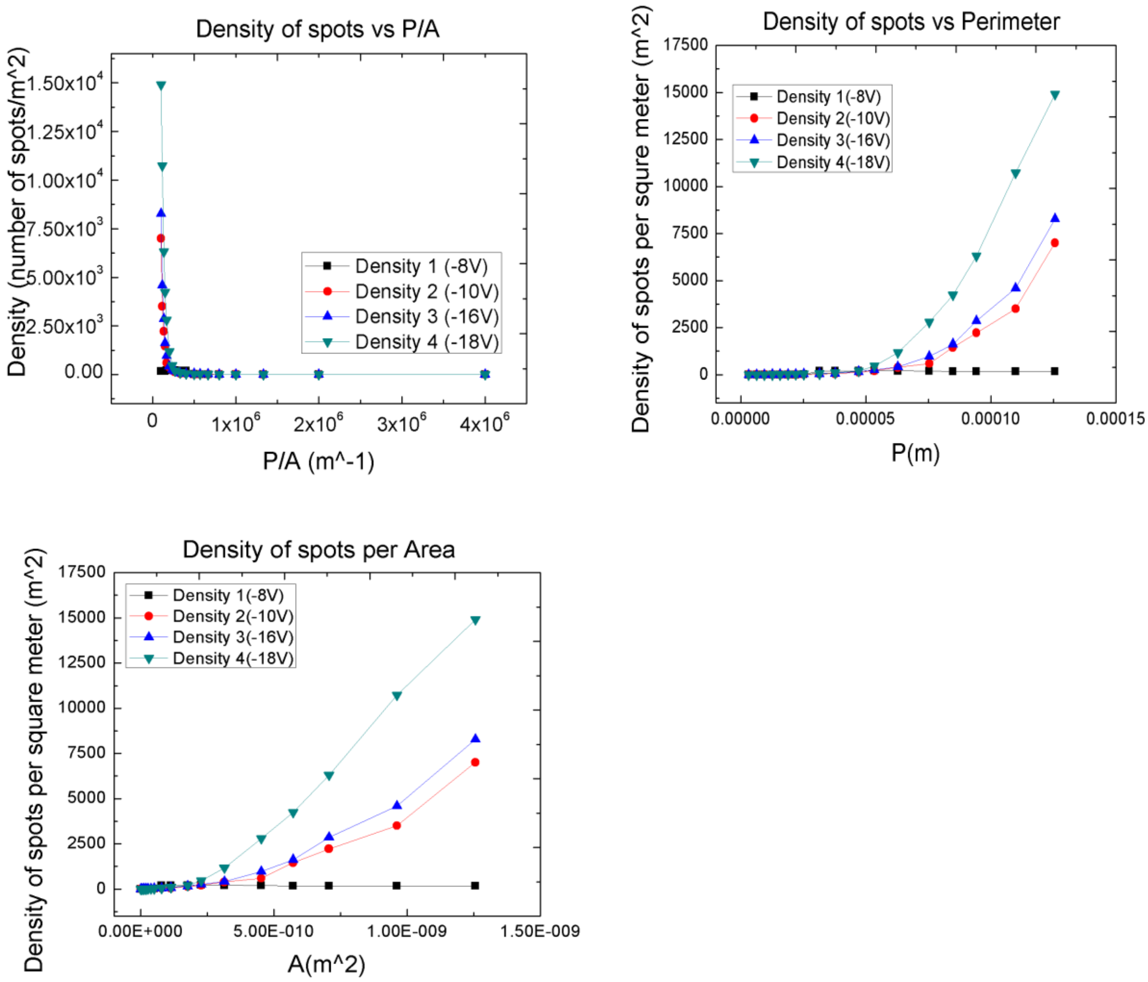

figure 27. Density of spots (number of spots/m^2) vs perimeter over area, perimeter and area for diodes from 40 to 1 µm.

As it can be seen, the number of spots increases in a big extent as the P/A decreases. The density of spots is a metric which gives information about the density of defects which is found to be much bigger for bigger diodes (due to larger active area). This information is relevant to the processing of the diode. The density of spots increases almost linearly with respect to the size (area and perimeter) of the diode. Increasing intensity and number of spots are noticed for rectangular diodes as well. The intensity vs size of circular diode (P/A and diameter) is:

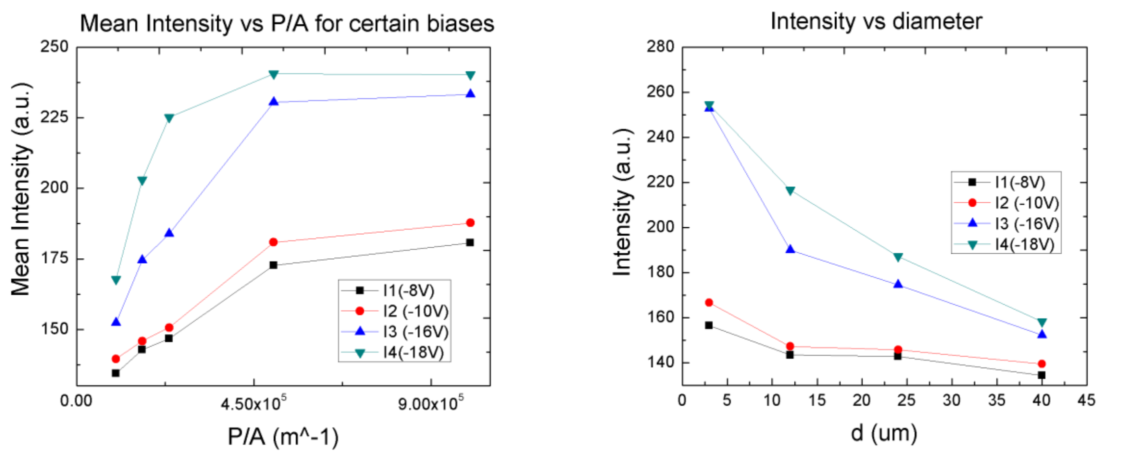

figure 28. Intensity vs perimeter over area and diameter for diodes from 40 to 1 µm. The standard deviation is from 2% to 7%.

As it can be seen from figure 28, the intensity increases as the ratio of the perimeter over the area increases. Thus intensity increases as the diameter of the diode decreases. This is in accordance with the higher electrical field expected in the smaller diodes. This is the evolution of the light radiation as the size of the diode increases at a fixed bias (-17 V):

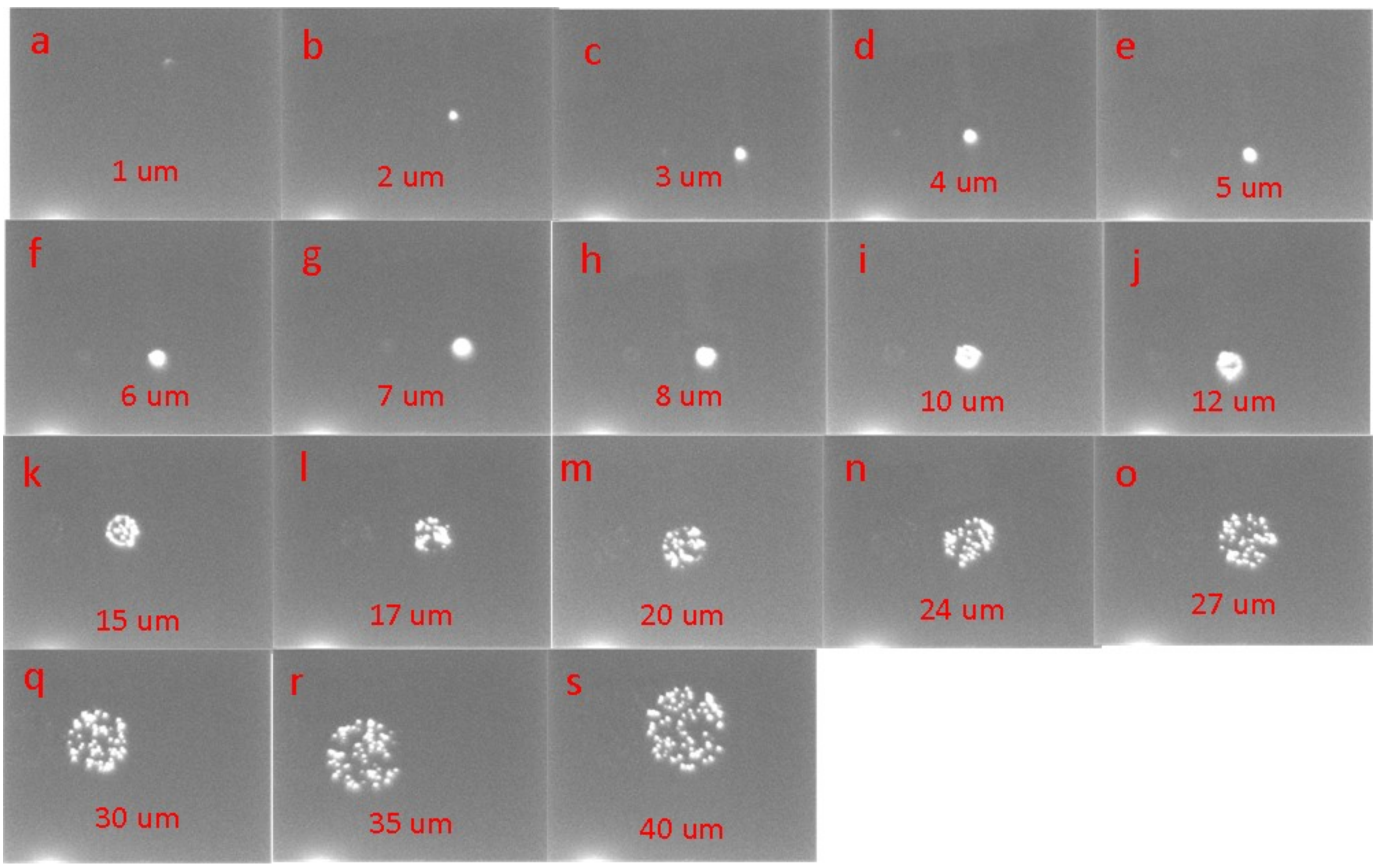

figure 29. The visible radiation (**a** to **s**) at a fixed bias (-17 V) for all available sizes of circular diodes.

As it can be seen from figure 29, the visible radiation from diodes with diameter of 1 to 10 µm looks like one big single spot. From diodes of 12 to 40 µm, it is possible to see separate light spots. The case of diodes of 1 to 10 μm with a single radiation spot could be attributed to very close spaced spots and the limited resolution of the lens (714 nm).

Another behavior that has to be mentioned is the formation of a ring around the diode perimeter when the bias reaches 24 V. The dots appearing around the diode perimeter connect to a line as it is depicted at figure 30 (diode with a diameter of 40 μm):

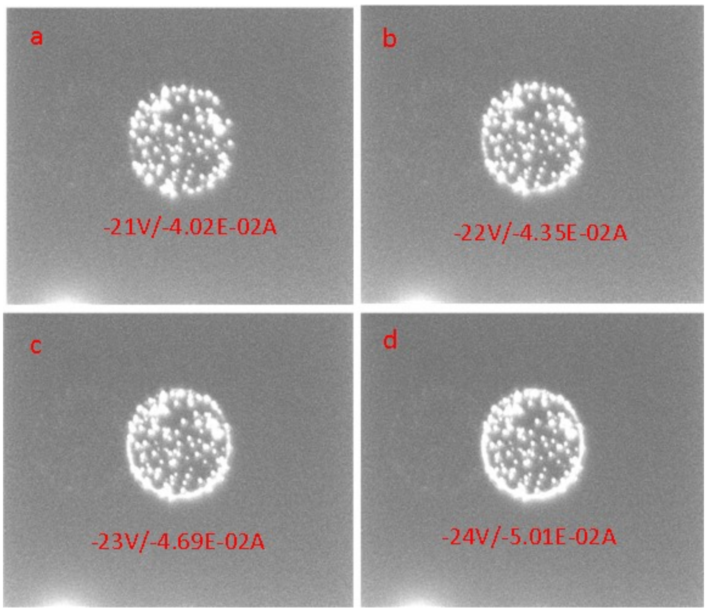

figure 30. Ring formation around the diode perimeter (**a** to **d**). Ring visible at 24 V (last picture-d).

Ring formation is noticed starting at lower bias (-18 V for diode of 24 μm) than 24 V for diodes of smaller size (<24 μm):

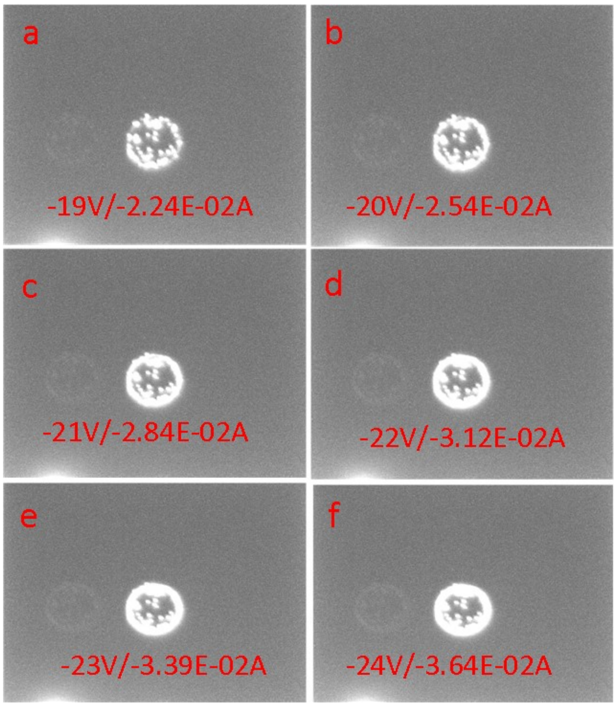

figure 31. Ring formation (**a** to **f**) starting from -19 V to -24 V (24 μm diode).

For diodes with a diameter of 12 μm down to 1 μm a glow developed around the diode is noticed which fully covers the surface of the diode as bias increases (figure 32):

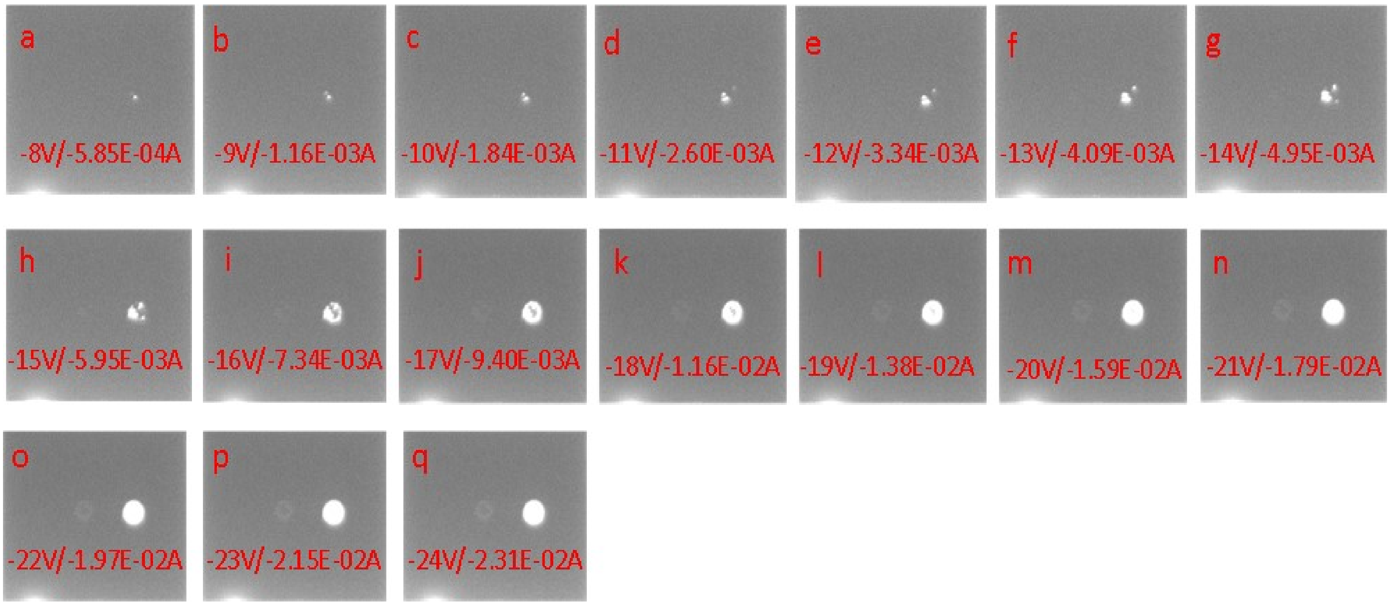

figure 32. Emission for incremented bias (a to q) from -8 to -24V (diode with diameter of 12 μm).

Full light all along the surface of the diode is emitted at a high bias (from -18 to -24V). This behavior could be attributed to a few light spots which emit more radiation as the bias increases or to the generation of more spots due to higher bias which cannot be discriminated due to limited resolution of the lens used (714 nm).

6.3 Visible and infrared emission

Another experiment conducted to investigate the performance of diode is supplying the same amount of DC power (forward bias: 5V/3.61E-02A and reverse bias: -12.5V/-1.44E-02A) in forward and reverse bias and attempting to compare the intensity (number of photons) of infrared and visible emissions respectively. It was found that this comparison is not feasible due to the fact that the visible and IR camera are not properly calibrated. Despite this pitfall, the comparison of the visible and IR emission in terms of series resistance gave useful information about the overall performance of the DUT in next chapters. The experiment of the actual comparison between the visible and the infrared emission for the same DC input power can be repeated in the future when the cameras are properly calibrated. This is how the two emissions look like (figure 33):

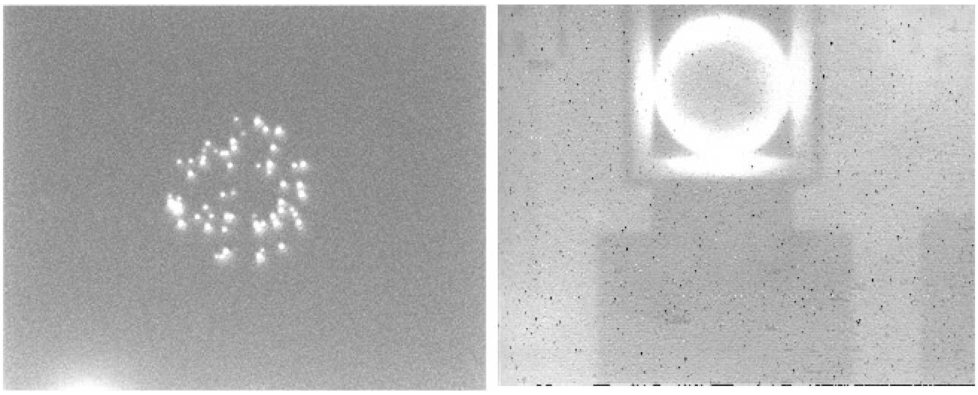

figure 33. Visible (left) vs infrared (right) emission (diode 40 μm/1.5 μm).

This experiment is repeated for diodes with diameters of 35, 30 and 27 μm for different anode size of 1.5, 1 and 0.5 μm. The results indicate that the same IR glow appears in all cases. This IR glow is found in other cases at Silicon LEDS in the literature **[26]**.

The measurements results analyzed so far refer to diodes with a breakdown voltage of 7 V. The next measurement refers to the second sort of diode available on the wafer with a breakdown voltage of 14 V.

6.4 Diodes with a breakdown voltage of -14 V

The diodes with a breakdown voltage of 14 V show a different behavior than the other ones with a breakdown voltage of 7 V. The reverse bias (avalanche state) does not give scattered visible light spots but a glow around the perimeter of the diode. On the other hand, the forward infrared emission shows light emission along the whole surface of the diode. These are the visible and infrared emission for 14 V diodes (figure 34):

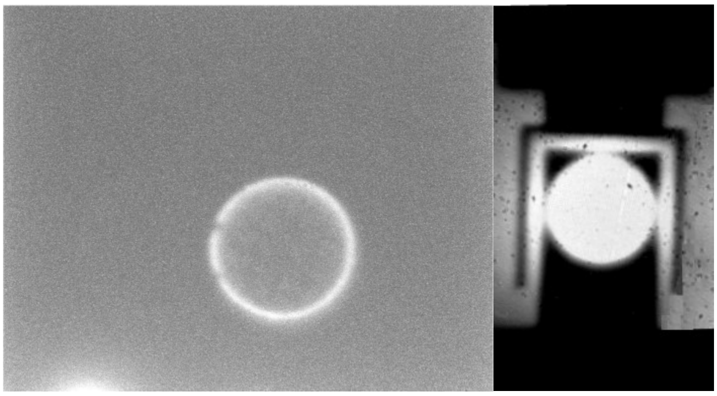

figure 34. Left: visible emission **right:** infrared emission**.**

The infrared emission occurs at 5 V/5.00E-02 A while the visible one at -16 V/-7.43E-03 A.

I-V characteristics for four diode sizes of 40, 24, 12 and 3 μm (with breakdown voltage of -14 V) are shown at figure 35:

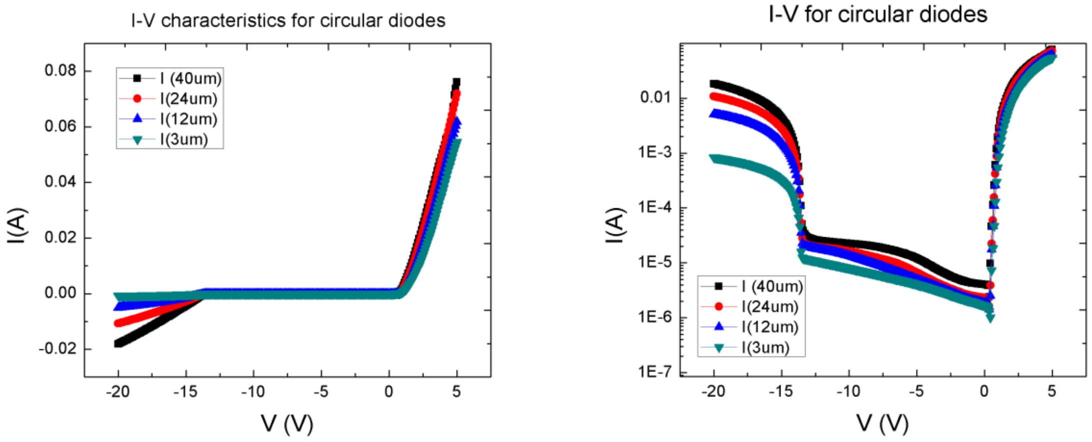

figure 35. I-V characteristics for diodes with diameter of 40, 24, 12 and 3 µm (breakdown voltage of 14V). Left: linear scale and right: log scale.

As it can be seen from figure 35, the I-V characteristics show a breakdown voltage near to -14 V. The slope of the I-V characteristic is bigger for diodes with bigger size. The breakdown is hardly visible at the diode of 3 µm where the effective resistance seems to be quite big. On the other hand, the log-scale I-V characteristic gives a more complete picture of the breakdown.

The visible glow appearing for diodes with a breakdown voltage of -14 V in avalanche mode can be better presented by showing the variation of the intensity across a notional line going through the center of the circular diode (figure 36):

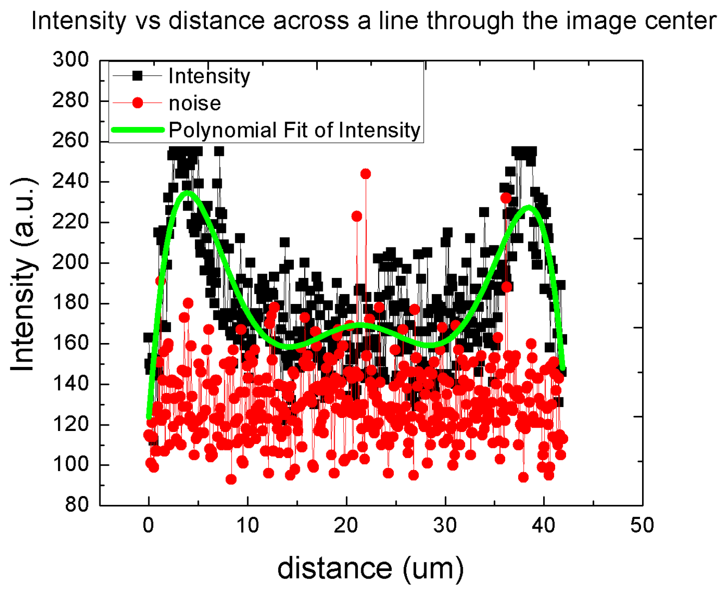

figure 36. Intensity variation for a line of pixels going through the diode center (40 µm diameter). Noise floor is also shown. Six orders polynomial fit is applied on the intensity showing a quite good match with the experimental data.

As it can be seen from figure 36, there are two peaks in the intensity where the visible radiation glow appears. The intensity falls towards the center of the diode where it slightly increases again. The intensity level towards the center is comparable to the noise floor of the image taken. Therefore the light mainly comes from the radiation glow around the perimeter of the diode and not from the area of the circular diode. This visible peripheral radiation glow is attributed to the high peripheral electrical field due to significantly less defects at the diodes with a breakdown voltage of -14 V.

There is current crowding at the perimeter of the diode while the potential (electrical field as well) fall towards the diode center (figure 37):

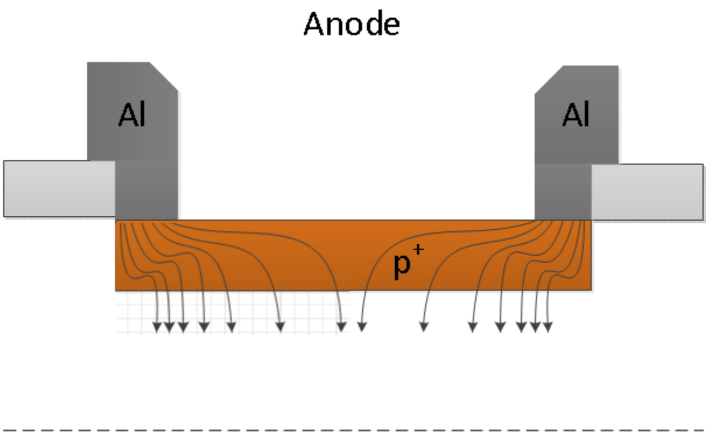

figure 37. Diode cross-section (V_{BR}=-14 V). Current crowding at the perimeter of the circular Si diode. The potential and the electrical field drop towards the diode center.

The infrared radiation observed at figure 34 (right) is well-known in literature for Si LEDs **[27]**. The light in the forward bias is not generated where the electrical field is the strongest but it is related to the mean free path of the excess minority carriers.

6.5 Series resistance

Series resistance is calculated (Appendices E and F) for all sizes of the circular diode in order to explain further the peripheral IR glow appearing during the forward bias for diodes of 7 V, the peripheral visible glow of 14 V diodes at reverse bias and the uniform IR light emission during the forward bias of 14 V diodes. The forward and reverse series resistance used within this report is expressed (Appendices E and F) as a ratio of ΔV/ΔI taking the difference of voltage over current (Appendix C) for two spots in the forward region (forward series resistance) and two in the reverse region (reverse series resistance). The series resistance dependence is better visualized in figure 38:

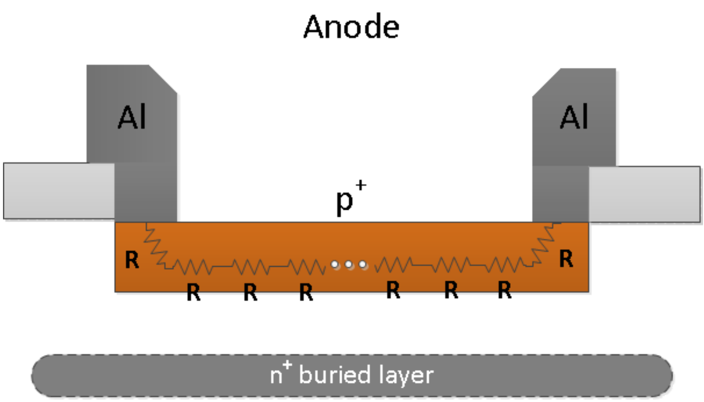

figure 38. Diode cross-section with series resistance visualized at the p^+ layer (V_{BR}=-7 V).

In figure 38, the series resistance at the p^+ layer is visualized where it is apparent that the potential (electrical field as well) decreases towards the center of the diode due to additional voltage drop across the horizontal (lateral) series resistance components.

The series resistance (forward and reverse) is plotted in three ways: versus perimeter, area and ratio of perimeter over area (figure 39):

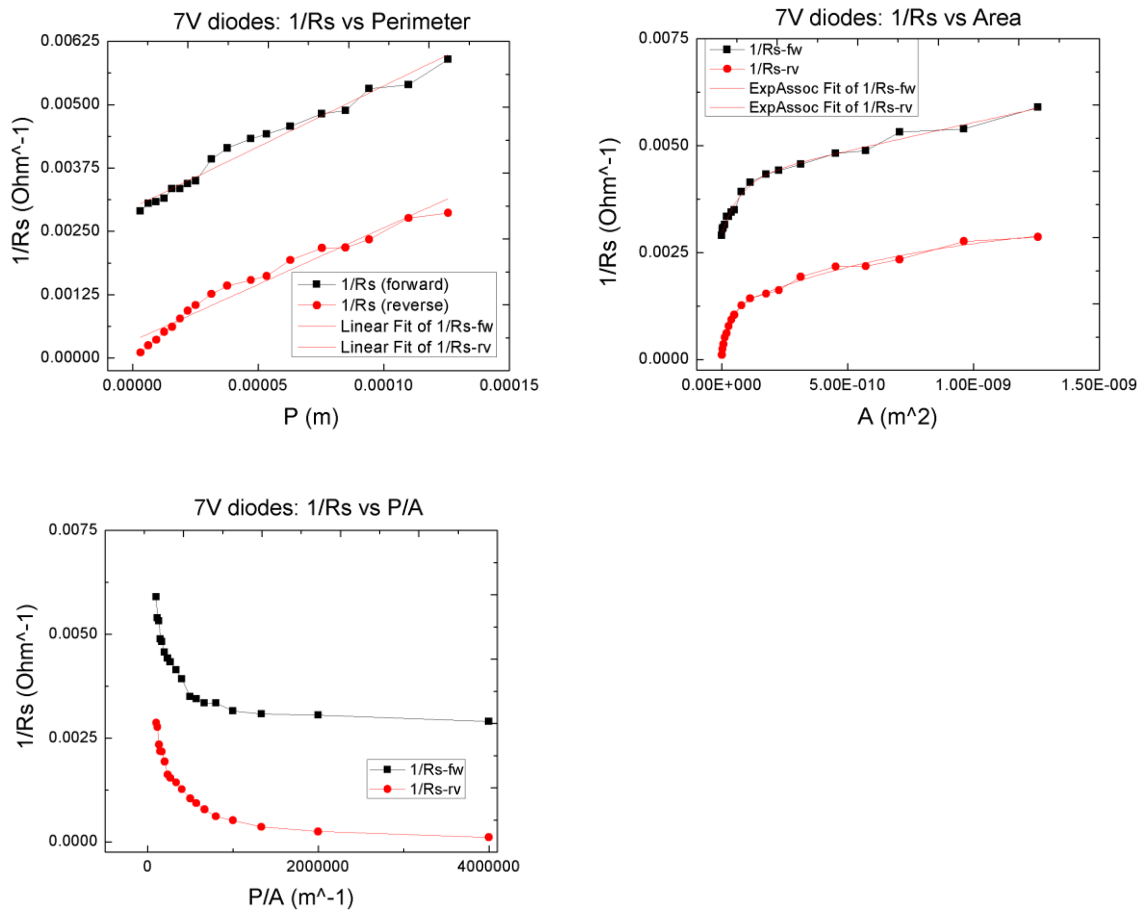

figure 39. Series resistance of circular diodes with a breakdown voltage of 7 V versus perimeter (top left), area (top right) and the ratio of perimeter over area (bottom left).

It can be seen (figure 39) that the series resistance (inverse) increase linearly as the perimeter of the circular diode increases. An almost logarithmic dependence is indicated for the series resistance versus area. The series conductance decreases almost exponentially as the P/A increases.

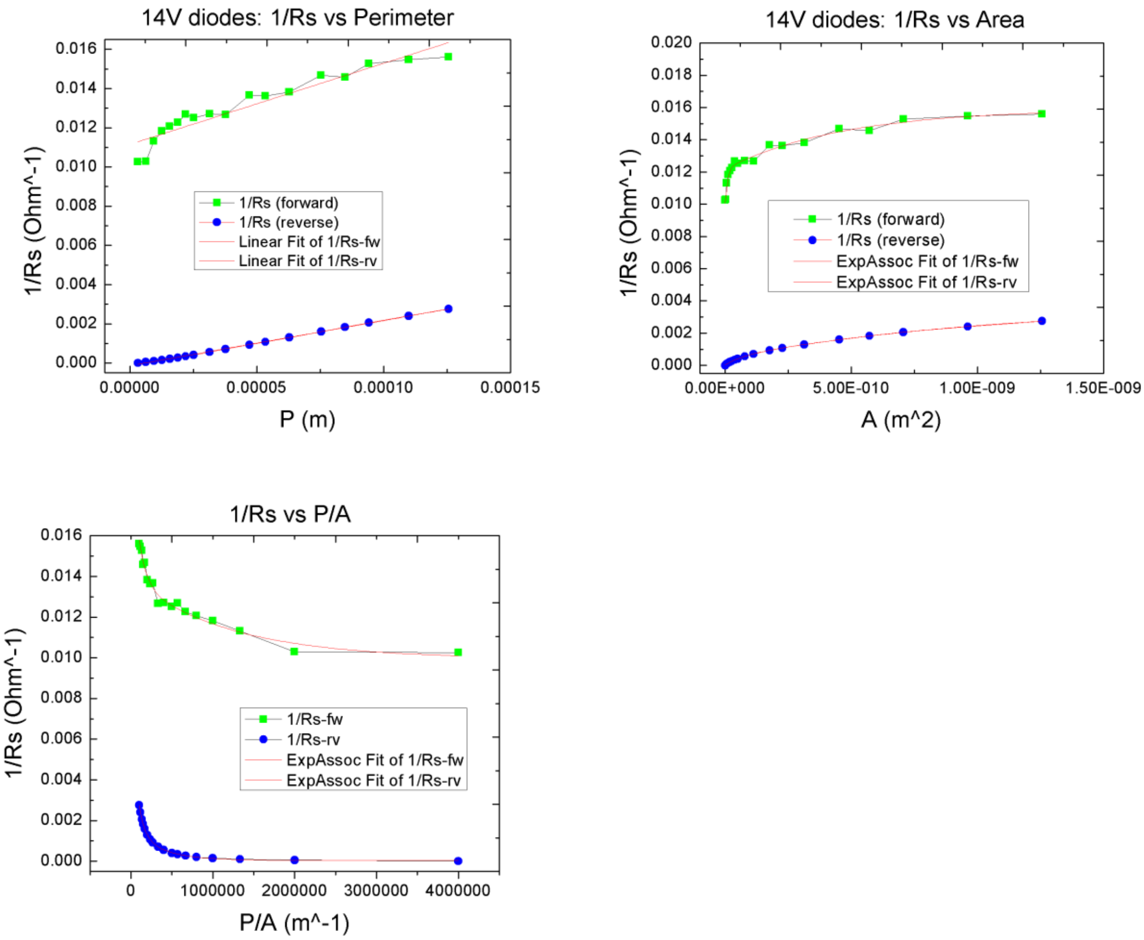

figure 40. Series resistance of circular diodes with a breakdown voltage of 14 V (top) versus perimeter (top left), area (top right) and the ratio of perimeter over area (bottom left).

From figure 40, it can be seen that there is a linear dependence of series conductance with respect to the perimeter. On the other hand, there is an almost logarithmic dependence of series conductance with respect to the area of the circular diode. A clear dependence of the series resistance on the size of the diode is indicated which is expected in theory. A comparative plot of the series conductance for 7 and 14 V diodes versus the perimeter is:

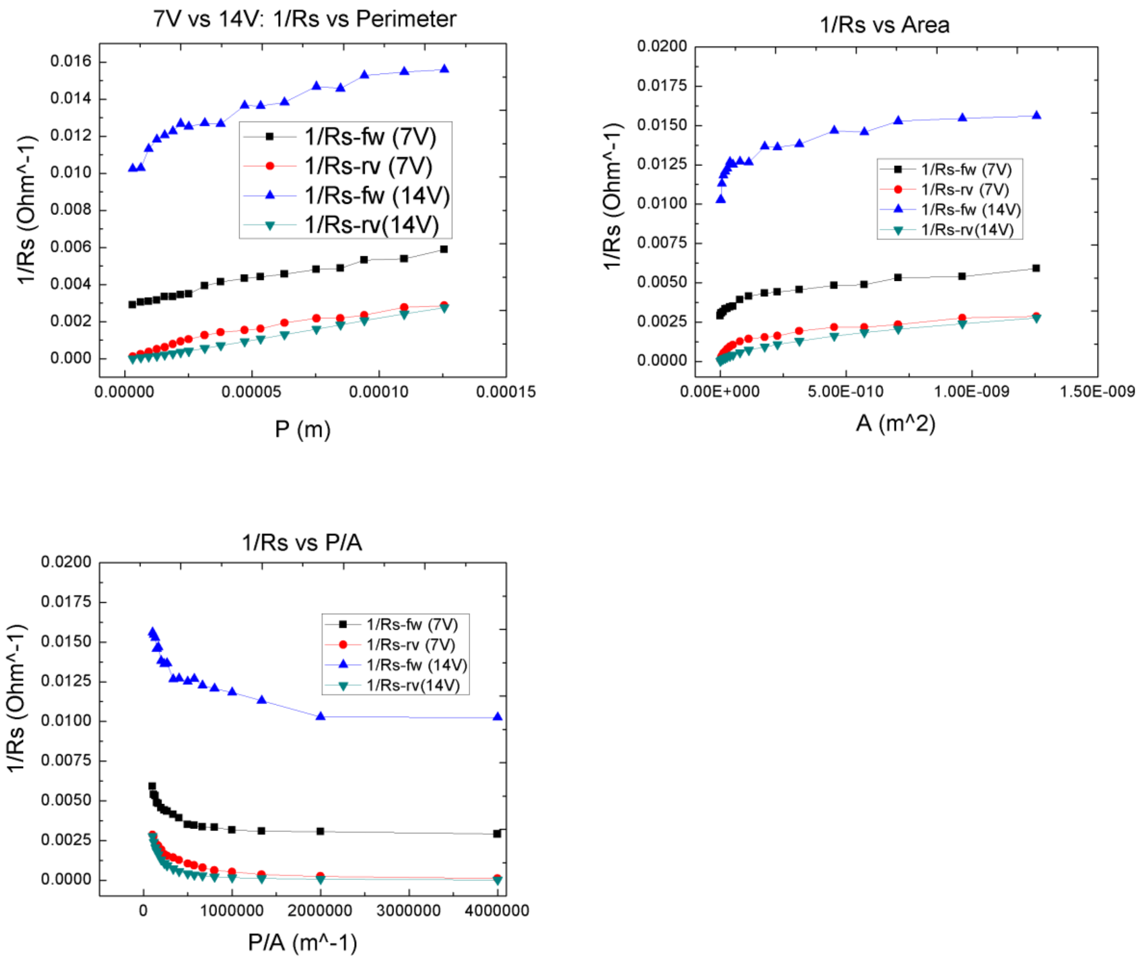

figure 41. Comparative plot of series conductance of 7 and 14 V versus perimeter, area and ratio of perimeter over area.

From figure 39, figure 40 and figure 41, we can conclude that there is carrier crowding at the perimeter so that the voltage drop is primarily over the edge of the anode. The indifference to the absence or presence of the n-buried layer shows that the sheet resistance of the p^+ layer dominates. This explains also the drop in intensity as the diodes get larger. The series conductance in forward for 14 V diodes is three times bigger than the other cases. This is understandable because the depletion of the p^+ region will be at its minimum. The 14 V forward case has a P-dependence that is more "logarithmic" than linear. This would mean that carrier crowding is not forcing all the current to flow at the perimeter and more is going through the central area than in the other cases. Together with the glow effect (from the large absorption length in the IR) this could account for the bright total surface for the IR measurement. The forward series resistance for diodes with a breakdown voltage of 14 V presents area dependence which is not linear. This is a clue that there should still be carrier crowding.

6.6 Peripheral and areal contribution to the total current

To study the current flows through a circular diode it can be helpful to express the total current as a sum of two components for a fixed bias: a peripheral and an areal current component. By assuming that the current distribution is laterally uniform, the current can then mathematically be expressed by the formula (1) where ***r*** is the radius of the circular diode:

$$(1)\ \mathbf{I} = \mathbf{P} * \boldsymbol{\alpha} + \mathbf{A} * \mathbf{b} = \mathbf{2} * \boldsymbol{\pi} * \mathbf{r} * \boldsymbol{\alpha} + \boldsymbol{\pi} * \mathbf{r}^{\mathbf{2}} * \mathbf{b}$$

If we divide (1) by $\boldsymbol{r}$ we get:

$$\mathbf{(2)}\ \mathbf{I/r} = \mathbf{2} * \boldsymbol{\pi} * \boldsymbol{\alpha} + \boldsymbol{\pi} * \mathbf{r} * \mathbf{b}$$

This equation is a straight line of the form $y = a * x + b$ (figure 42):

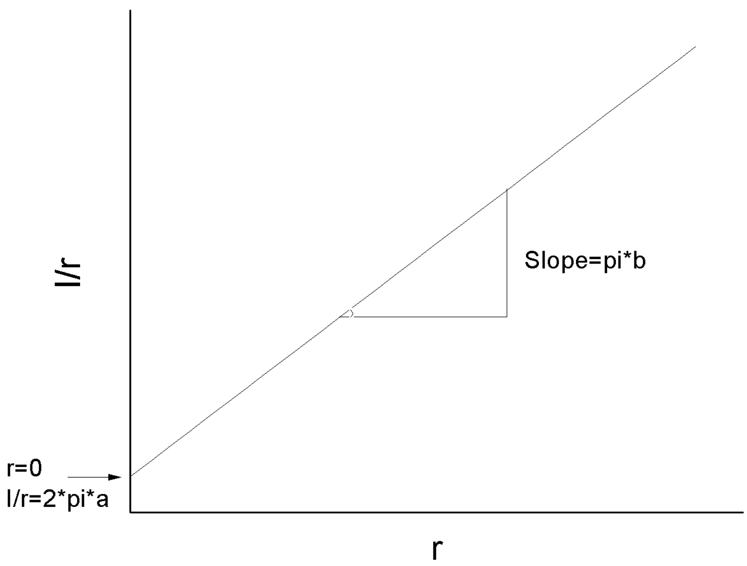

figure 42. Straight line of I/r versus r with its y-intercept and slope where *pi* is *π.*

The y-intercept of this line (figure 42) expresses the peripheral component of the current while the slope expresses the areal component of the total current. In reality the on-mask radius may be different from the actual radius after device processing. This is an effect that can lead to incorrect values for a and b.

The plot of I/r or 2I/d versus d is (figure 43):

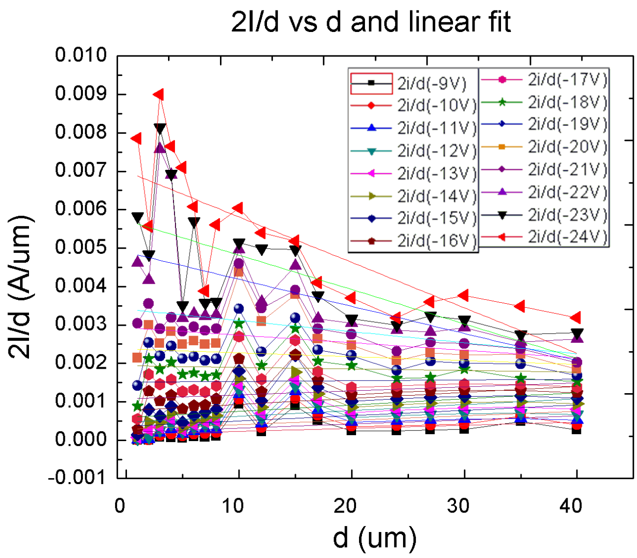

figure 43. 2I/d versus d at a fixed bias of -16 V for diodes with a breakdown voltage of 7 V.

As it can be seen from figure 43, there are several data points which deviate from a "straight" line (figure 42). This deviation becomes higher as the bias increases. It is reasonable to expect deviations from a straight line in view of the curvature and limited size of the small diodes. For the small devices the high curvature of the circular area means that the effective sheet resistance is higher than for the large devices therefore relatively higher current spreading exists in the small devices when the sheet resistance dominates for the high reverse voltages. The voltage drop from the perimeter to the central region may hardly play a role for the smaller devices therefore for low reverse bias this effect may dominate and cause relatively high current intensity. Both of these effects play a role on the deviations from the straight line. Despite these pitfalls, an attempt to fit the data points at figure 43 with linear fitting is made. The y-intercept and slopes of these lines are calculated and plotted in figure 44 :

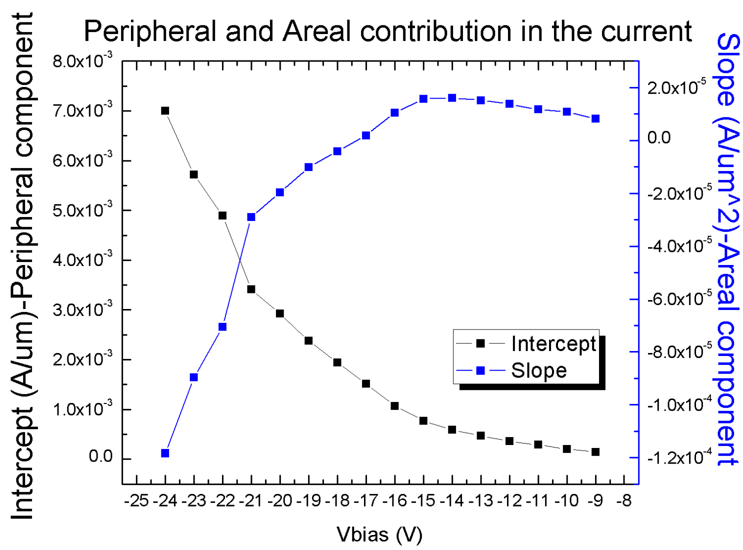

figure 44. y-intercept and slope of 2I/d versus d. The y-intercept expresses the peripheral current component while the slope expresses the areal current component.

From figure 44, it can be seen that the peripheral component dominates for all biases. The peripheral component increases for increasing bias while the areal component decreases. The figure 44 indicates the high contribution of the peripheral current to the total current. Another proof that the peripheral current dominates over the areal current is the plot shown at figure 45:

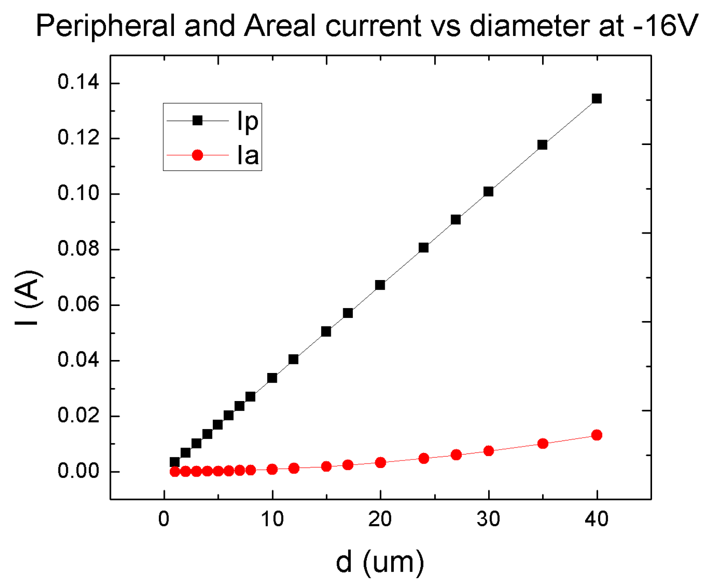

figure 45. Peripheral (I_p) and areal (I_a) current versus diameter for diodes with a breakdown voltage of 7 V at a fixed bias of -16 V. The peripheral current dominates.

The peripheral current dominates over the areal current. This is in accordance with the ring appearing around the perimeter of the diode for high biases. The total current coming from the analysis (formula **(**1**)**) approaches the total current measured.

For diodes with a breakdown voltage of -14 V, the 2I/d versus d for various biases is (figure 46):

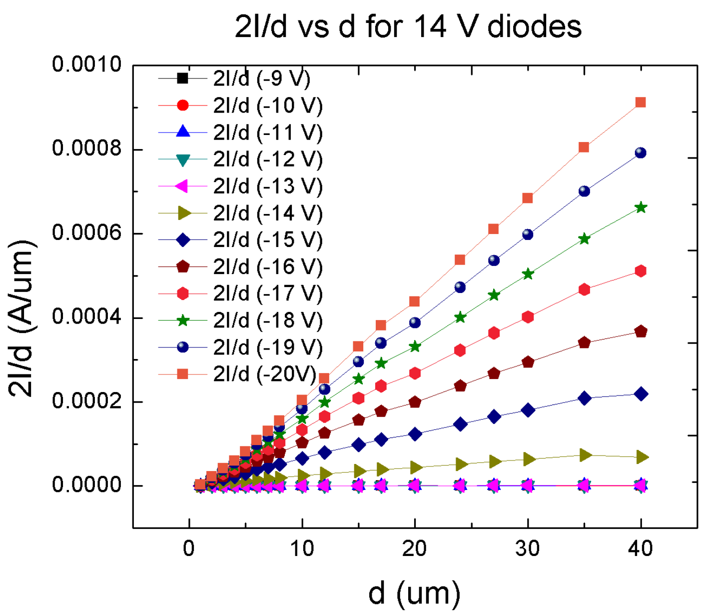

figure 46. 2I/d versus d for various biases for diodes with a breakdown voltage of -14 V.

The lines of 2I/d versus d are remarkably straight compared to those of diodes with a breakdown voltage of -7 V. The 14 V diodes have significantly less defects as already mentioned in previous chapters. By extracting the y-intercept and the slope of these lines we get the following plot (figure 47):

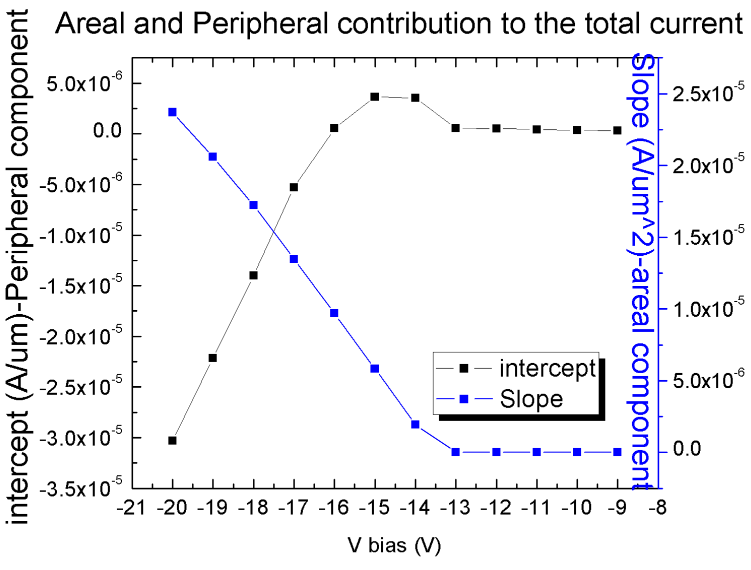

figure 47. Intercept and slope of 2I/d vs d for a breakdown voltage of -14 V.

From figure 47 it can be seen, that the peripheral and areal current components are stable until the breakdown and then the areal and peripheral current both increase (absolute values). The peripheral and areal currents with respect to the size of the diode (diameter) for a fixed bias of -16 V is:

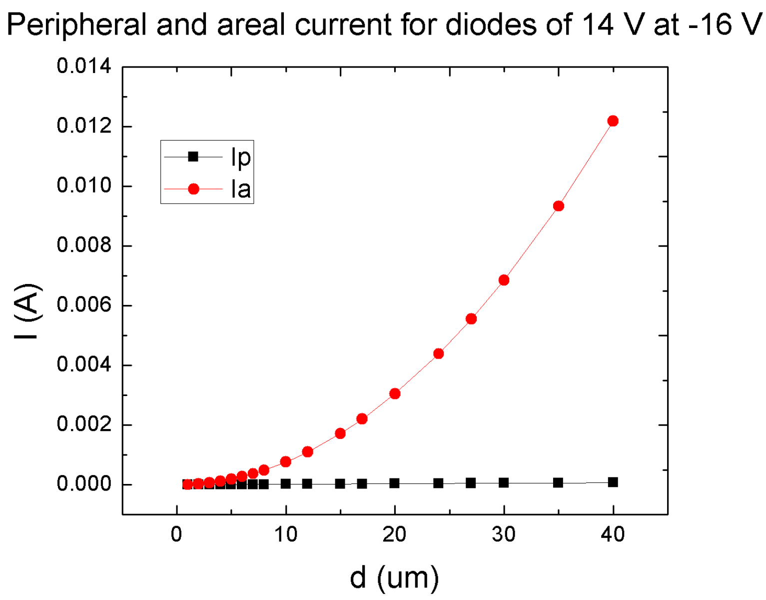

figure 48. The peripheral (I_p) and areal (I_a) current for diodes with a breakdown voltage of -14 V for a fixed bias of -16 V.

Based on the analysis chosen previously (where the total current is a summary of an areal and peripheral component of the form **(**1**)**), the areal current dominates over the peripheral current (figure 48). The visible radiation glow appearing at the avalanche mode for diodes with breakdown voltage of -14 V was attributed to the existence of high electrical field at the periphery due to current crowding as a result of the high sheet resistance. Unlike the 7 V breakdown devices, the lack of defects prevents light emission at lower reverse voltages where the series resistance is also lower. Current crowding is expected at the periphery of the circular diode. It has to be underlined that this domination of the areal current component is not expected. Normally, due to the visible radiation glow (figure 34) the peripheral current should dominate. These complications can lead to the conclusion that the current model should probably include more parameters in order to approach the real case such as the width of the piece at the perimeter that covers the part of the current that is not laterally uniform (ΔL). This ΔL may be higher for the 14 V breakdown device than for the 7 V device because the series resistance without the buried layer may be a bit lower. This is however, not obvious from figure 41, perhaps because the R_s is extracted at a voltage higher than that of the onset of the glowing ring.

To further investigate the behavior of the current for diodes with a breakdown voltage of -14 V, the perimeter dependence of the total current is examined again. This is the plot of the total current with respect to the perimeter of the circular diodes for a fixed bias of -16 V (for diodes with a breakdown voltage of -14 V):

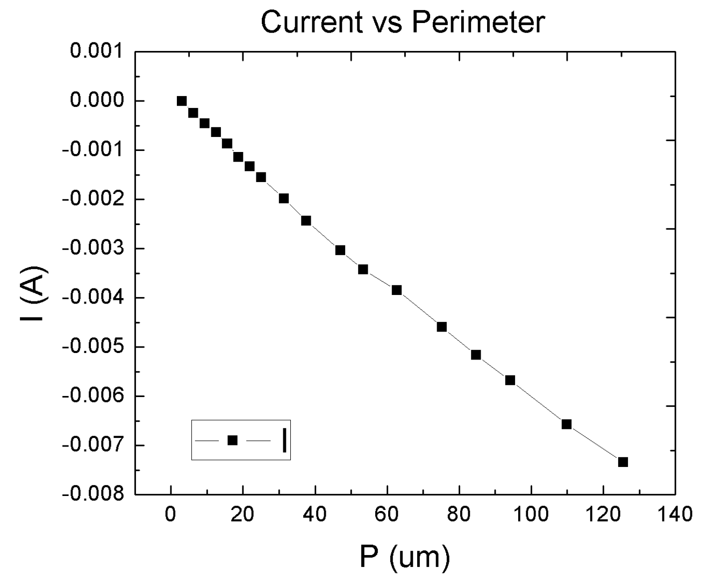

figure 49. Current versus perimeter at -16 V for diodes with breakdown voltage of -14 V.

From figure 49, it can be seen that the current is a linear function of the perimeter. This clue does indicate that the perimeter is hogging all the current over a distance that is small compared to the radius of the circular diode.

The areal current contributes to the low intensity light appearing towards the diode center (figure 36).

7. Discussion

Visible emission in avalanche Si diodes appears as scattered spots all along the active junction plane where $F > F_{crit}$. These spots always appear at the same location when the biasing is repeated in multiple cycles. This spatial invariance indicates a link between spots and crystal defects which can act as “gettering sites” for local field enhancement and current microfilamentation and hence serve as suitable recombination centres for photon emission. More spots are appearing when the bias is increased. The spot intensity increases as the size of the diode decreases. The spot density is very probably related t to the defect density in the diode which is found to be higher for larger diodes. The average intensity of the emission increases for higher bias levels.

Many diode sizes were measured. Bigger mean intensity is noticed for smaller diodes. The intensity of the spots close to the center of diodes increases for diodes with smaller diameter. Therefore the electric field is stronger towards the center for diodes of small diameter. The current density is higher for small diodes and this is also a reason higher intensity is noticed for small diodes. When bias exceeds a certain level, a light ring is formed around the perimeter of the diode. This ring is formed for diodes with smaller size at lower bias levels. This ring gradually turns into a full light coverage all along the diode for diodes of small diameter. Similar behavior for intensity and number of spots is noticed for diodes of rectangular shape for various sizes.

The infrared emission in diodes with a breakdown voltage of 7 V shows a glow around the diode. This glow could be attributed to a number of reasons. One possible explanation is that the B-Si bonds at the interface have a lower bonding energy than the bulk B-Si(4) bonds, hence generate a more IR spectrum (higher λ) than the bulk Si. Another possible statement is that the effective hole concentration in the Si at the surface increases with temperature and shifts the depletion edge into the Si. Therefore less light originating from the bulk Si is emitted from the surface. The IR bump from the interface becomes more dominant (as the bulk IR light does). The IR glow must be coming from deep bulk Si regions / regions under the oxide. It is blocked by the metal. This means that the field strength at the perimeter / in the depth is high enough to make IR emission possible but maybe less visual.

For diodes of breakdown voltage of 14 V, a visible emission which does not meet the standards of a “spotted” emission is observed. Instead, a visible light glow is formed around the perimeter of the diode. This could be attributed to the etching of the contact which has caused damage and the emission is defect-related but the analysis of the series resistance in the different cases indicates that it is much more likely that series resistance is also responsible for this effect. The 14 V devices have very few defects compared to the 7 V devices due to the absence of a buried layer. Apparently, there is no defect breakdown (light from points at a relatively low reverse bias) and the "ideal" breakdown mechanism is governing the light emission. The infrared emission in diodes with a breakdown voltage of 14 V is a full light emission all along the surface of the diode. In the diodes of 14 V breakdown voltage with the lighter n-region doping, the depletion of the holes at the PureB interface will be less and the lateral series resistance will be lower. This would lead to less current crowding at the contact ring and a more uniform light emission in forward.

Regarding the series resistance, a dependence on the size of the diode is clearly shown. An almost linear dependence on the perimeter is indicated. An almost “logarithmic” dependence is indicated on the area of the diode. Perimeter current crowding is considered responsible for the visible and infrared glow appearing in the 14 and 7 V diodes respectively. The lower series resistance in the forward region for 14 V diodes is responsible for the full coverage of diodes by light in the IR range. The series resistance of 14 V was expected to be much higher than the series resistance of the 7 V diodes due to absence of buried layer. On the contrary, the (reverse) series resistance was found to be comparable in both cases. This led to the consideration that the sheet resistance of the p^+ layer dominates.

The analysis of the areal and peripheral current for circular diodes (formula (1)) with a breakdown voltage of -7 V indicated the domination of the peripheral current over the areal component. This clue is in accordance with the ring appearing for circular diodes of 24 µm at high biases (-24 V). On the other hand, the same current model indicates areal current domination over the peripheral component for diodes with a breakdown voltage of -14 V. This is opposed to the expectation that there is current crowding and higher electrical field at the periphery of the diode which cause the visible radiation glow at avalanche mode. The absence of the n^+-buried layer in the diodes with a breakdown voltage of -14 V indicates significantly less defects. This contradiction of the current model (formula (1)) towards the theoretical expectations of a dominating peripheral current component indicates that probably more parameters should be taken into account in order to express the total current as a summary of a peripheral and an areal component, such as a region of width ΔL at the perimeter where (area dependent component is not constant). To further investigate the dependence of the total current on the size of the circular diode, we plot the current versus the diode perimeter. This graph shows the linear dependence of the current to the perimeter of the diode. This behavior indicates that the perimeter is hogging all the current over a distance that is small compared to the radius.

Fewer spots are expected for small diodes due to smaller active area. The dark count rate for small diodes can be very sparse. This feature makes them ideal for SPADs (Single Photon Avalanche Diodes) since avalanche should be triggered by light detection and not from defects. On the contrary, the many (defects) light spots in the big diodes make them more proper for LEDs (Light Emitting Diodes). A recommendation for the future is the material analysis of the defects causing the generation of light such as using SEM to scan for Si stacking faults.

8. Conclusions

Synchronized electrical and optical measurement has been achieved. The operation of the setup has been confirmed through experiments. Fixed defects exist in the diodes. This is proved through repeated avalanche cycles which show the same arrangement of visible light spots. The number of visible spots increases as the bias increases. The density of spots increases for diodes with bigger diameter. The average intensity increases as the bias levels increase. Higher intensity is noticed for diodes of smaller size due to stronger electric field and current density. The small avalanche Si diodes are proper for SPADs and the big ones for LEDs. The explanation of the IR glow for diodes of 7 V breakdown voltage and the visible-IR emission for diodes of 14 V breakdown voltage has been attempted in this report but remain open for further investigation in the future.

Appendix A

The software developed within this project consists of two separate processes: one is for Keithley 4200 SCS and the other one for the camera. The inter-process communication is implemented through semaphores.

Two basic C modules were developed which correspond to the experiments conducted within this project: the “cycles” and “steps” Keithley 4200 SCS modules. The 1st one is for experiment #1 and the 2nd one for experiment #2. Additional C++ modules were developed for the operation of the camera in parallel with Keithley 4200 SCS.

It has to be underlined that the “cycles” and “steps” modules are adjusted to work with **SMU2**. The code of the Keithley 4200 SCS and camera modules is stored in the archive of the SC (Semiconductor Components) group.

Appendix B

In this appendix, the mean and standard deviation values of intensity (arbitrary units) and current (A) of diodes with a breakdown voltage of 7 V for varying bias (V) are included. Next, the mean and standard deviation values of intensity (first) and current (next) for diodes of 40, 35, 30, 27 µm are mentioned:

			Vbias-mean intesity																
A/A	**diameter (um)**	**a r l width (um)**	-8	-9	-10	-11	-12	-13	-14	-15	-16	-17	-18	-19	-20	-21	-22	-23	-24
1	40	1.5	134.4280143	136.9017	139.5523	141.8821	143.7048	145.2032	146.9595	149.4071	152.3281	155.4251	158.3137	161.3048	164.8512	167.7232	168.4535	171.3583	172.7736
2	35	1.5	133.9204167	137.1891	140.0412	143.4655	146.0083	147.8944	149.7774	151.9578	154.5125	157.5519	161.0161	161.2389	164.7261	168.2276	171.4793	173.9452	166.9799
3	30	1.5	132.250475	134.5618	136.8508	139.6069	142.8294	146.374	149.6132	152.4581	155.1082	157.6847	161.1188	165.5205	170.3771	174.5474	176.7906	175.2841	169.2696
4	27	1.5	131.4357125	134.8511	137.8457	141.7203	144.8584	148.3564	151.4501	153.9419	156.0196	158.0081	160.226	160.7427	165.0445	168.3158	170.9804	173.7063	169.9549
5	40	1	133.90275	137.0241	139.5828	142.9855	146.6271	150.2738	153.3538	155.7029	157.3331	158.7441	160.1993	162.2035	163.841	166.6386	166.4155	167.9215	161.159
6	35	1	130.4472714	135.2036	137.3406	140.6267	144.4398	148.4368	152.0669	155.2252	157.9135	160.2732	162.6744	165.3602	167.1143	165.8183	168.02	164.5451	166.0484
7	30	1	132.39674	136.84	138.9789	141.1855	143.5923	145.8565	148.1045	150.526	153.1027	155.805	158.7061	162.536	168.3938	165.5062	163.7028	159.6581	156.1632
8	27	1	131.7672857	135.6099	138.4648	141.7565	145.3255	148.655	151.5106	154.0723	156.4239	158.6072	161.4114	165.2801	171.7116	176.3486	179.2681	181.3253	177.2421
9	40	0.5	131.9581143	135.8275	138.4039	140.725	143.1397	145.5159	147.9714	150.1569	151.7899	153.327	155.1857	157.7658	161.0214	164.7076	168.0813	170.8791	167.3773
10	35	0.5	131.8534833	136.735	139.2391	141.6583	144.262	146.8803	149.4823	152.3612	155.2622	158.8133	160.4719	162.7651	165.3234	168.4406	171.8236	174.6485	172.4464
11	30	0.5	133.46305	136.4275	138.4401	140.8322	143.2472	145.6372	147.6332	149.3498	151.0301	152.6455	154.8459	158.2435	162.5944	165.6568	166.8336	169.1966	170.106
12	27	0.5	131.0202714	135.053	138.3491	142.2007	145.9389	149.1576	151.9499	154.0931	155.9347	157.3512	158.6436	161.4733	165.4212	168.1985	168.6437	169.9946	171.9428

			Vbias-standard deviation																
A/A	**diameter (um)**	**a r l width (um)**	-8	-9	-10	-11	-12	-13	-14	-15	-16	-17	-18	-19	-20	-21	-22	-23	-24
1	40	1.5	2.127928386	4.963675	5.701715	6.015685	6.01022	6.090365	6.037288	6.165468	6.258506	6.472929	6.855095	7.595847	8.551533	10.06273	16.58455	18.06356	19.02168
2	35	1.5	3.051975093	5.420553	4.974592	5.533071	6.056376	6.195035	6.402454	6.930989	7.342266	7.278446	7.062296	12.68546	13.45209	14.68843	15.16121	15.66178	18.64413
3	30	1.5	3.337089095	1.979088	2.715292	3.858214	5.031408	6.00058	6.434662	6.017826	5.281886	4.967232	5.214564	5.264088	5.540665	5.926716	6.933342	15.45491	23.3352
4	27	1.5	5.10679597	5.759377	6.425236	7.855053	8.80942	9.407705	9.371593	8.874991	8.199067	7.552618	6.769824	9.186134	10.26269	12.57738	14.14793	15.04187	20.50394
5	40	1	6.846218014	5.694864	5.86729	6.499831	6.936806	7.099155	6.370196	5.512329	4.861391	4.318437	3.888499	4.176447	5.588682	8.472769	10.21074	13.79141	17.49648
6	35	1	3.520764358	4.366783	4.123387	4.676192	5.544924	6.148914	6.257613	5.851778	5.545787	5.665434	6.248758	6.908592	9.011274	14.12503	15.06296	18.72952	19.9617
7	30	1	2.924194139	6.286295	7.008383	7.605965	7.646566	7.18003	6.807161	6.623386	6.667315	6.806699	7.228492	7.950062	8.841435	14.23601	17.77145	15.10997	16.63021
8	27	1	2.594801995	3.214532	3.889911	4.975211	5.693555	5.936986	6.266518	7.023877	8.124651	9.111165	9.662522	9.739992	9.539112	9.714935	10.17474	11.90646	20.82156
9	40	0.5	5.135391397	4.428755	3.588686	3.314439	3.742313	4.582612	5.252638	5.461257	5.468598	5.688464	6.319571	6.9231	7.39413	7.656775	7.984374	8.193051	13.80407
10	35	0.5	4.655181914	4.577327	3.511425	2.89862	3.379152	4.258079	4.76257	5.27051	5.801244	5.969614	5.964537	5.374534	5.058096	4.934328	4.943589	4.812474	8.832598
11	30	0.5	4.310068286	3.704339	2.605756	2.593909	3.672427	4.75037	5.258733	5.429262	5.439179	5.492163	5.523103	5.908422	6.856171	9.564723	14.74086	14.76782	16.75409
12	27	0.5	3.478267439	4.099237	4.430305	4.64324	4.475665	4.211922	4.670683	5.317276	5.587636	5.927434	6.575607	7.358204	7.464404	7.558537	10.76978	13.52671	12.10244

			i-mean intesity																
A/A	ameter (u	l width (u	-8	-9	-10	-11	-12	-13	-14	-15	-16	-17	-18	-19	-20	-21	-22	-23	-24
1	40	1.5	-3.01E-03	-5.41E-03	-7.94E-03	-1.06E-02	-1.33E-02	-1.61E-02	-1.89E-02	-2.18E-02	-2.47E-02	-2.76E-02	-3.05E-02	-3.36E-02	-3.69E-02	-4.04E-02	-5.27E-02	-5.60E-02	-6.38E-02
2	35	1.5	-4.26E-03	-8.58E-03	-1.09E-02	-9.91E-03	-1.24E-02	-1.49E-02	-1.75E-02	-2.01E-02	-2.27E-02	-2.54E-02	-2.81E-02	-3.47E-02	-3.91E-02	-4.17E-02	-4.48E-02	-4.81E-02	-6.10E-02
3	30	1.5	-2.38E-03	-4.24E-03	-6.24E-03	-8.30E-03	-1.04E-02	-1.26E-02	-1.48E-02	-1.71E-02	-1.95E-02	-2.19E-02	-2.78E-02	-3.00E-02	-3.34E-02	-3.77E-02	-4.40E-02	-4.69E-02	-5.66E-02
4	27	1.5	-1.93E-03	-3.54E-03	-5.27E-03	-7.09E-03	-9.02E-03	-1.10E-02	-1.30E-02	-1.51E-02	-1.73E-02	-1.95E-02	-2.20E-02	-2.77E-02	-3.07E-02	-3.44E-02	-3.80E-02	-4.37E-02	-4.87E-02

			i-standard deviation																
A/A	ameter (u	l width (u	-8	-9	-10	-11	-12	-13	-14	-15	-16	-17	-18	-19	-20	-21	-22	-23	-24
1	40	1.5	0.000432	0.000669	0.000947	0.001235	0.001515	0.001743	0.001899	0.002027	0.002103	0.002112	0.002058	0.001831	0.001402	0.00098	0.016633	0.016487	0.019014
2	35	1.5	0.004707	0.010692	0.010908	0.002265	0.002507	0.002719	0.002863	0.002966	0.002994	0.00292	0.002756	0.012205	0.015014	0.01288	0.012168	0.012057	0.018923
3	30	1.5	0.000352	0.000451	0.000529	0.000611	0.000674	0.000713	0.000792	0.000856	0.00092	0.000972	0.010455	0.008784	0.009401	0.012535	0.014548	0.014474	0.01706
4	27	1.5	0.000228	0.000353	0.000491	0.000638	0.000774	0.000895	0.00099	0.001035	0.001052	0.001029	0.000886	0.008779	0.00849	0.010222	0.011951	0.013378	0.013976

Next, the mean and standard deviation of intensity and current values of diodes with diameter of 24, 20, 17, 15, 12 and 10 μm follow:

			Vbias-mean intesity															
A/A	eter	a r l width (um)	-9	-10	-11	-12	-13	-14	-15	-16	-17	-18	-19	-20	-21	-22	-23	-24
1	24	1.5	142.79057	145.8404	150.3179	154.9689	159.5741	164.1832	169.121	174.5078	180.3455	187.2766	196.3908	197.506	203.0105	206.8908	202.2131	201.0619
2	20	1.5	141.43409	144.9758	149.3561	153.9192	159.0304	164.9547	171.61	178.8153	185.4769	192.0229	200.8592	206.668	210.7895	213.4922	210.4042	207.7098
3	17	1.5	146.80308	150.6031	155.5096	162.0851	166.327	171.6797	177.395	183.9789	193.699	204.5552	214.2964	220.639	225.1396	225.9027	211.5357	210.5085
4	15	1.5	149.94544	151.5828	155.9396	160.4175	165.025	168.8875	174.051	179.5432	188.9851	200.1222	207.7086	211.55	212.7974	206.6534	208.7526	198.6607
5	12	1.5	143.4796	147.2773	153.0313	159.2572	165.9397	172.8886	179.735	189.9416	205.4911	216.6389	217.565	218.797	221.2653	214.8048	202.5832	195.9803
6	10	1.5	136.82761	139.1273	142.9215	148.2761	154.4604	162.9484	171.701	190.8616	201.7616	209.6229	205.2845	206.179	207.1867	207.8054	206.9369	191.8154

			Vbias-standard deviation															
A/A	eter	a r l width (um)	-9	-10	-11	-12	-13	-14	-15	-16	-17	-18	-19	-20	-21	-22	-23	-24
1	24	1.5	10.85367624	9.033411	8.044678	7.312439	6.849917	6.944118	7.11062	6.753403	6.107593	4.933097	4.116784	21.1293	22.84891	22.95037	29.35073	35.03976
2	20	1.5	8.427275668	7.165969	6.689504	6.242609	5.738319	5.221826	5.2365	5.405344	9.80642	21.10918	23.5986	25.3008	24.91397	24.62512	29.28623	35.72163
3	17	1.5	10.74010486	10.28076	10.75414	12.31577	11.33168	10.44772	9.28801	6.892821	5.829302	4.637002	3.515236	3.38635	3.512647	5.840333	37.46818	36.6163
4	15	1.5	20.04732859	18.82815	19.01275	19.05152	19.08458	19.79131	19.904	21.78049	26.07723	30.63021	33.51909	37.0846	36.82148	44.39312	43.80227	49.13996
5	12	1.5	7.026141089	7.541717	8.56627	8.517423	7.473593	6.80345	6.29992	5.797071	5.582704	6.036428	16.02379	24.29	25.89546	34.32058	41.75648	46.3855
6	10	1.5	3.78142899	4.441926	7.651826	11.37018	13.59271	15.044	16.9857	24.95171	33.12017	32.62429	36.9937	40.4353	42.46912	43.85042	45.88933	48.97979

			i-mean intesity															
A/A	diameter (um)	a r l width (um)	-9	-10	-11	-12	-13	-14	-15	-16	-17	-18	-19	-20	-21	-22	-23	-24
1	24	1.5	-2.93E-03	-4.43E-03	-6.02E-03	-7.66E-03	-9.34E-03	-1.11E-02	-1.29E-02	-1.48E-02	-1.69E-02	-1.93E-02	-2.18E-02	-2.48E-02	-2.78E-02	-3.45E-02	-3.60E-02	-3.83E-02
2	20	1.5	-2.41E-03	-3.60E-03	-4.75E-03	-5.89E-03	-7.23E-03	-8.54E-03	-1.01E-02	-1.18E-02	-1.38E-02	-1.94E-02	-2.20E-02	-2.47E-02	-2.75E-02	-3.04E-02	-3.15E-02	-3.71E-02
3	17	1.5	-4.30E-03	-5.44E-03	-6.61E-03	-7.81E-03	-8.95E-03	-1.03E-02	-1.17E-02	-1.33E-02	-1.52E-02	-1.75E-02	-1.99E-02	-2.24E-02	-2.47E-02	-2.69E-02	-3.20E-02	-3.49E-02
4	15	1.5	-6.72E-03	-8.09E-03	-9.47E-03	-1.05E-02	-1.18E-02	-1.33E-02	-1.66E-02	-1.67E-02	-1.95E-02	-2.18E-02	-2.39E-02	-2.85E-02	-2.93E-02	-3.41E-02	-3.72E-02	-3.89E-02
5	12	1.5	-1.27E-03	-1.93E-03	-2.64E-03	-3.37E-03	-4.19E-03	-5.12E-03	-6.16E-03	-7.54E-03	-9.50E-03	-1.17E-02	-1.38E-02	-1.85E-02	-2.06E-02	-2.16E-02	-2.99E-02	-3.24E-02
6	10	1.5	-4.69E-03	-5.29E-03	-5.97E-03	-6.55E-03	-7.26E-03	-8.01E-03	-9.02E-03	-1.06E-02	-1.35E-02	-1.52E-02	-1.71E-02	-2.19E-02	-2.30E-02	-2.48E-02	-2.57E-02	-3.02E-02

			i-mean intesity															
A/A	diameter (um)	a r l width (um)	-9	-10	-11	-12	-13	-14	-15	-16	-17	-18	-19	-20	-21	-22	-23	-24
1	24	1.5	0.000391	0.000538	0.000692	0.000811	0.000905	0.000971	0.001008	0.000995	0.000985	0.000859	0.001138	0.001158	0.00114	0.010896	0.007344	0.006668
2	20	1.5	0.000702	0.000858	0.001079	0.001115	0.001264	0.001536	0.001639	0.001709	0.001696	0.010255	0.010102	0.009761	0.010149	0.011046	0.007152	0.011609
3	17	1.5	0.007381	0.007915	0.008408	0.008818	0.009199	0.009456	0.009617	0.009678	0.009557	0.009291	0.008922	0.008561	0.008228	0.007992	0.011725	0.013358
4	15	1.5	0.008599	0.009206	0.009756	0.010353	0.010801	0.011161	0.013313	0.011821	0.013337	0.013344	0.012377	0.015738	0.013587	0.014529	0.015669	0.015438
5	12	1.5	0.00031	0.000438	0.000522	0.000587	0.000626	0.00065	0.000632	0.000521	0.00045	0.000445	0.000446	0.00804	0.008441	0.005975	0.013025	0.011588
6	10	1.5	0.00784	0.008456	0.008915	0.009147	0.009479	0.009704	0.00975	0.009572	0.011184	0.01063	0.010654	0.012889	0.011994	0.012338	0.011526	0.012968

Next the mean and standard deviation values of intensity and current for diodes of 8 down to 1 µm follow:

			Vbias-mean intesity															
A/A	eter	a r l width (um)	-9	-10	-11	-12	-13	-14	-15	-16	-17	-18	-19	-20	-21	-22	-23	-24
1	8	1.5	161.0226	173.3732	186.6622	198.457	208.3399	218.2816	232.886	240.5284	243.44	245.4499	246.7131	247.75	242.4474	222.5932	169.4091	
2	7	1.5	159.804225	170.801	181.2327	190.3895	193.9341	209.1735	232.214	238.6077	237.3444	225.2952	226.2623	226.579	233.531	223.1129	218.6798	
3	6	1.5	155.001975	161.0951	168.0638	176.0229	186.8111	211.4782	230.641	239.0533	243.0013	245.4005	247.0172	246.723	221.4032	222.1904	220.2398	
4	5	1.5	142.7051	149.3472	162.1016	172.2989	188.012	227.1865	242.97	248.9596	251.4329	252.5994	253.274	253.738	254.0088	225.9947	226.3396	
5	4	1.5	162.240675	175.9449	187.0453	196.4327	205.9742	223.2701	235.774	241.3793	244.3835	246.2033	243.2664	230.124	234.0612	216.6244	221.0059	
6	3	1.5	151.9509	164.8692	177.1162	187.967	202.1944	228.557	241.951	247.5947	250.1469	251.5324	228.0904	228.04	232.071	229.6646	211.0519	
7	2	1.5	130.059975	130.9214	131.4575	131.6331	155.9257	194.9119	213.738	223.966	230.0807	233.9108	236.4786	238.298	237.9534	237.5054	236.3761	
8	1	1.5	124.4701333	124.4522	125.1301	126.1892	127.6182	132.1115	147.816	160.0996	170.1557	177.897	183.5549	188.343	193.2149	188.1747	185.7731	

			Vbias-standard deviation															
A/A	eter	a r l width (um)	-9	-10	-11	-12	-13	-14	-15	-16	-17	-18	-19	-20	-21	-22	-23	-24
1	8	1.5	11.07440646	10.72103	9.023397	9.270733	10.49625	7.880898	5.33866	6.85236	5.886142	4.814231	4.265315	3.97241	11.28786	38.11298	46.72519	
2	7	1.5	8.19883049	11.1299	14.42323	16.93843	23.14132	21.9681	16.7993	16.23218	13.49829	32.7514	32.81157	33.823	23.58066	42.00705	49.88819	
3	6	1.5	21.11902564	23.08338	24.18765	22.94835	16.7344	7.138414	8.75942	7.848851	7.205247	6.489837	5.859992	4.9333	48.18724	48.27669	50.73902	
4	5	1.5	13.18969741	19.34652	24.22761	28.80944	25.37721	8.344241	6.47268	4.541356	3.326196	2.484648	1.902256	1.44319	1.133841	48.89916	48.33321	
5	4	1.5	20.62640436	21.70907	19.0255	15.27483	11.4056	4.621375	4.84975	5.498869	5.250523	4.475797	6.216613	30.5769	25.65369	33.10891	51.80953	
6	3	1.5	16.91638181	22.04188	27.14475	31.23006	25.69529	12.267	7.04878	4.9205	3.760273	3.061984	44.49942	45.3466	38.87641	33.75194	43.66082	
7	2	1.5	4.170081172	3.843273	3.356559	3.786576	6.443549	4.221772	5.1726	6.395525	6.83143	6.888314	6.938952	6.73182	8.74224	9.291773	10.2388	
8	1	1.5	0.728781016	2.807654	4.167982	5.018431	5.55827	8.486336	9.96265	11.31087	12.3036	12.06797	10.86361	9.43433	9.646705	8.969835	7.852831	

i-mean intesity

A/A	diameter (um)	a r l width (um)	-9	-10	-11	-12	-13	-14	-15	-16	-17	-18	-19	-20	-21	-22	-23	-24
1	8	1.5	-4.03E-04	-7.61E-04	-1.14E-03	-1.56E-03	-2.02E-03	-2.55E-03	-3.25E-03	-4.29E-03	-5.65E-03	-6.80E-03	-8.46E-03	-1.01E-02	-1.16E-02	-1.30E-02	-1.44E-02	-2.24E-02
2	7	1.5	-2.65E-04	-6.02E-04	-9.65E-04	-1.32E-03	-1.69E-03	-2.08E-03	-2.54E-03	-3.19E-03	-4.38E-03	-5.82E-03	-7.25E-03	-8.71E-03	-9.99E-03	-1.13E-02	-1.25E-02	-1.36E-02
3	6	1.5	-2.54E-04	-4.52E-04	-6.95E-04	-9.36E-04	-1.22E-03	-1.54E-03	-1.94E-03	-2.69E-03	-3.93E-03	-5.26E-03	-6.54E-03	-7.74E-03	-8.85E-03	-9.88E-03	-1.71E-02	-1.83E-02
4	5	1.5	-1.22E-04	-2.55E-04	-3.95E-04	-5.33E-04	-6.51E-04	-8.31E-04	-1.15E-03	-2.04E-03	-3.16E-03	-4.27E-03	-5.30E-03	-6.22E-03	-7.08E-03	-7.93E-03	-8.78E-03	-1.78E-02
5	4	1.5	-1.32E-04	-3.13E-04	-5.62E-04	-8.23E-04	-1.11E-03	-1.42E-03	-1.77E-03	-2.33E-03	-3.15E-03	-4.05E-03	-4.89E-03	-5.66E-03	-6.39E-03	-1.38E-02	-1.39E-02	-1.53E-02
6	3	1.5	-1.02E-04	-1.77E-04	-2.76E-04	-3.88E-04	-5.13E-04	-6.90E-04	-9.43E-04	-1.52E-03	-2.18E-03	-2.77E-03	-3.29E-03	-3.77E-03	-4.35E-03	-1.14E-02	-1.22E-02	-1.35E-02
7	2	1.5	-6.82E-07	-7.27E-06	-1.76E-05	-7.69E-05	-2.64E-04	-4.74E-04	-7.98E-04	-1.27E-03	-1.71E-03	-2.13E-03	-2.53E-03	-2.99E-03	-3.55E-03	-4.17E-03	-4.84E-03	-5.57E-03
8	1	1.5	-3.70E-08	-8.39E-08	-1.18E-06	-1.62E-05	-3.65E-05	-5.39E-05	-7.04E-05	-1.41E-04	-2.75E-04	-4.43E-04	-7.10E-04	-1.07E-03	-1.52E-03	-2.31E-03	-2.91E-03	-3.93E-03

i-standard deviation

A/A	diameter (um)	a r l width (um)	-9	-10	-11	-12	-13	-14	-15	-16	-17	-18	-19	-20	-21	-22	-23	-24
1	8	1.5	0.000208	0.000251	0.000314	0.000401	0.000488	0.000586	0.000688	0.000782	0.000817	0.000163	0.000171	0.000201	0.000212	0.000253	0.0003	0.011945
2	7	1.5	5.16E-05	8.74E-05	0.000135	0.000216	0.000286	0.000349	0.000393	0.000363	0.000221	0.000193	0.000188	0.000267	0.00029	0.000363	0.000471	0.000533
3	6	1.5	0.000221	0.000336	0.000425	0.000512	0.000585	0.000614	0.000552	0.000295	0.000276	0.000322	0.00036	0.000397	0.000433	0.000468	0.010481	0.010804
4	5	1.5	3E-05	5.08E-05	9.08E-05	0.00017	0.000225	0.000297	0.000244	0.00017	0.000216	0.000265	0.000313	0.000375	0.000437	0.000493	0.000577	0.014557
5	4	1.5	0.000147	0.000234	0.000315	0.000359	0.000378	0.000434	0.000498	0.000452	0.000424	0.0005	0.000606	0.000696	0.000793	0.012411	0.011351	0.012487
6	3	1.5	2.94E-05	4.22E-05	5.99E-05	8.85E-05	0.000127	0.000174	0.000192	0.00025	0.000303	0.000368	0.000447	0.000544	0.000677	0.011507	0.011857	0.012804
7	2	1.5	1.09E-06	1.24E-05	2.88E-05	9.56E-05	0.000362	0.00067	0.000921	0.001123	0.001385	0.001625	0.001829	0.001994	0.002103	0.002183	0.002263	0.002328
8	1	1.5	2.82E-08	7.34E-08	1.53E-06	1.69E-05	2.85E-05	4.02E-05	5.17E-05	0.00013	0.000205	0.000296	0.000362	0.0004	0.000422	0.00082	0.000799	0.001219

Appendix C

The series resistance of the 7 V and 14 V diodes are the differential resistance calculated from two points of the I-V curve in the forward region (forward resistance) and two points from the reverse region (reverse resistance):

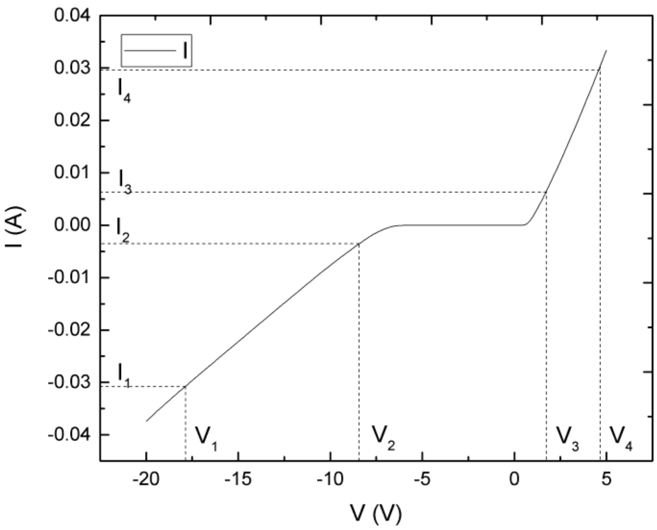

figure 50. I-V curve from a 7 V diode and the points used for the series resistance calculations.

Therefore the forward resistance is expressed as $R_{fw} = (V_4 - V_3)/(I_4 - I_3)$ and the reverse resistance as $R_{rv} = (V_2 - V_1)/(I_2 - I_1)$.

The I-V measurements used for these calculations are stored in the Semiconductor Components archive.

Appendix D

A sample of the matlab program used for the calculation of the average intensity out of the images captured (in arbitrary units) is:

```
numfiles = 19;
mydata = cell(1, numfiles);
for k = 1:numfiles
  myfilename = sprintf('E:\\Continuation_MSc thesis\\backup\\backup 
15.12 only new files\\15.12\\c\\8.1.5\\img%d.bmp', k);
  mydata{k} = importdata(myfilename);
end
for j = 1:numfiles
  mean_a{j}=mean2(imcrop(mydata{j}, [473.5 349.5 92 42]));
end

for k = 1:numfiles
  myfilename = sprintf('E:\\Continuation_MSc thesis\\backup\\backup 
15.12 only new files\\15.12\\c\\7.1.5\\img%d.bmp', k);
  mydata{k} = importdata(myfilename);
end
for j = 1:numfiles
  mean_b{j}=mean2(imcrop(mydata{j}, [219.5 545.5 54 76]));
end

for k = 1:numfiles
  myfilename = sprintf('E:\\Continuation_MSc thesis\\backup\\backup 
15.12 only new files\\15.12\\c\\6.1.5\\img%d.bmp', k);
  mydata{k} = importdata(myfilename);
end
for j = 1:numfiles
  mean_c{j}=mean2(imcrop(mydata{j}, [395.5 503.5 66 62]));
end

for k = 1:numfiles
  myfilename = sprintf('E:\\Continuation_MSc thesis\\backup\\backup 
15.12 only new files\\15.12\\c\\5.1.5\\img%d.bmp', k);
  mydata{k} = importdata(myfilename);
end
for j = 1:numfiles
  mean_d{j}=mean2(imcrop(mydata{j}, [669.5 369.5 60 58]));
end

for k = 1:numfiles
  myfilename = sprintf('E:\\Continuation_MSc thesis\\backup\\backup 
15.12 only new files\\15.12\\c\\4.1.5\\img%d.bmp', k);
  mydata{k} = importdata(myfilename);
end
for j = 1:numfiles
  mean_e{j}=mean2(imcrop(mydata{j}, [513.5 427.5 46 50]));
end

for k = 1:numfiles
  myfilename = sprintf('E:\\Continuation_MSc thesis\\backup\\backup 
15.12 only new files\\15.12\\c\\3.1.5\\img%d.bmp', k);
```

```
  mydata{k} = importdata(myfilename);
end
for j = 1:numfiles
  mean_f{j}=mean2(imcrop(mydata{j}, [561.5 341.5 28 36]));
end

for k = 1:numfiles
  myfilename = sprintf('E:\\Continuation_MSc thesis\\backup\\backup
15.12 only new files\\15.12\\c\\2.1.5\\img%d.bmp', k);
  mydata{k} = importdata(myfilename);
end
for j = 1:numfiles
  mean_g{j}=mean2(imcrop(mydata{j}, [727.5 505.5 36 36]));
end

for k = 1:numfiles
  myfilename = sprintf('E:\\Continuation_MSc thesis\\backup\\backup
15.12 only new files\\15.12\\c\\1.1.5\\img%d.bmp', k);
  mydata{k} = importdata(myfilename);
end
for j = 1:numfiles
  mean_h{j}=mean2(imcrop(mydata{j}, [513.5 385.5 26 30]));
end

mean_a
mean_b
mean_c
mean_d
mean_e
mean_f
mean_g
mean_h
```

Appendix E

A sample of the matlab program used for the calculation of the series resistance for diodes with breakdown voltage of 7 V (with diameter from 8 to 1 μm) is:

```
A_data = dataset('xlsfile','E:\Continuation_MSc thesis\backup\backup
15.12 only new files\15.12\a\8.1.5\vrd#1@1.csv');

Rsfw_8_a=(A_data{1,3}-A_data{68,3})/(A_data{1,2}-A_data{68,2})

Rsrv_8_a=(A_data{147,3}-A_data{280,3})/(A_data{147,2}-A_data{280,2})

B_data = dataset('xlsfile','E:\Continuation_MSc thesis\backup\backup
15.12 only new files\15.12\a\7.1.5\vrd#1@1.csv');

Rsfw_7_a=(B_data{1,3}-B_data{68,3})/(B_data{1,2}-A_data{68,2})
```

```
Rsrv_7_a=(B_data{147,3}-B_data{280,3})/(B_data{147,2}-B_data{280,2})

C_data = dataset('xlsfile','E:\Continuation_MSc thesis\backup\backup 15.12 only new files\15.12\a\6.1.5\vrd#1@1.csv');

Rsfw_6_a=(C_data{1,3}-C_data{68,3})/(C_data{1,2}-C_data{68,2})

Rsrv_6_a=(C_data{147,3}-C_data{280,3})/(C_data{147,2}-C_data{280,2})

D_data = dataset('xlsfile','E:\Continuation_MSc thesis\backup\backup 15.12 only new files\15.12\a\5.1.5\vrd#1@1.csv');

Rsfw_5_a=(D_data{1,3}-D_data{68,3})/(D_data{1,2}-D_data{68,2})

Rsrv_5_a=(D_data{147,3}-D_data{280,3})/(D_data{147,2}-D_data{280,2})

E_data = dataset('xlsfile','E:\Continuation_MSc thesis\backup\backup 15.12 only new files\15.12\a\4.1.5\vrd#1@1.csv');

Rsfw_4_a=(E_data{1,3}-E_data{68,3})/(E_data{1,2}-E_data{68,2})

Rsrv_4_a=(E_data{147,3}-E_data{280,3})/(E_data{147,2}-E_data{280,2})

F_data = dataset('xlsfile','E:\Continuation_MSc thesis\backup\backup 15.12 only new files\15.12\a\3.1.5\vrd#1@1.csv');

Rsfw_3_a=(F_data{1,3}-F_data{68,3})/(F_data{1,2}-F_data{68,2})

Rsrv_3_a=(F_data{147,3}-F_data{280,3})/(F_data{147,2}-F_data{280,2})

G_data = dataset('xlsfile','E:\Continuation_MSc thesis\backup\backup 15.12 only new files\15.12\a\2.1.5\vrd#1@1.csv');

Rsfw_2_a=(G_data{1,3}-G_data{68,3})/(G_data{1,2}-G_data{68,2})

Rsrv_2_a=(G_data{147,3}-G_data{280,3})/(G_data{147,2}-G_data{280,2})

H_data = dataset('xlsfile','E:\Continuation_MSc thesis\backup\backup 15.12 only new files\15.12\a\1.1.5\vrd#1@1.csv');

Rsfw_1_a=(H_data{1,3}-H_data{68,3})/(H_data{1,2}-H_data{68,2})

Rsrv_1_a=(H_data{147,3}-H_data{280,3})/(H_data{147,2}-H_data{280,2})
```

Appendix F

A sample of the matlab program used for the calculation of series resistance for diodes with breakdown voltage of 14 V (with diameter from 40 to 1 µm) is:

```
A_data = dataset('xlsfile','E:\Continuation_MSc thesis\backup\backup
03.02 new files only\03.02\a\40\vrd#1@1.csv');

Rsfw_40_a=(A_data{1,3}-A_data{46,3})/(A_data{1,2}-A_data{46,2})

Rsrv_40_a=(A_data{225,3}-A_data{280,3})/(A_data{225,2}-
A_data{280,2})

B_data = dataset('xlsfile','E:\Continuation_MSc thesis\backup\backup
03.02 new files only\03.02\a\35\vrd#1@1.csv');

Rsfw_35_a=(B_data{1,3}-B_data{46,3})/(B_data{1,2}-A_data{46,2})

Rsrv_35_a=(B_data{225,3}-B_data{280,3})/(B_data{225,2}-
B_data{280,2})

C_data = dataset('xlsfile','E:\Continuation_MSc thesis\backup\backup
03.02 new files only\03.02\a\30\vrd#1@1.csv');

Rsfw_30_a=(C_data{1,3}-C_data{46,3})/(C_data{1,2}-C_data{46,2})

Rsrv_30_a=(C_data{225,3}-C_data{280,3})/(C_data{225,2}-
C_data{280,2})

D_data = dataset('xlsfile','E:\Continuation_MSc thesis\backup\backup
03.02 new files only\03.02\a\27\vrd#1@1.csv');

Rsfw_27_a=(D_data{1,3}-D_data{46,3})/(D_data{1,2}-D_data{46,2})

Rsrv_27_a=(D_data{225,3}-D_data{280,3})/(D_data{225,2}-
D_data{280,2})

E_data = dataset('xlsfile','E:\Continuation_MSc thesis\backup\backup
03.02 new files only\03.02\a\24\vrd#1@1.csv');

Rsfw_24_a=(E_data{1,3}-E_data{46,3})/(E_data{1,2}-E_data{46,2})

Rsrv_24_a=(E_data{225,3}-E_data{280,3})/(E_data{225,2}-
E_data{280,2})

F_data = dataset('xlsfile','E:\Continuation_MSc thesis\backup\backup
03.02 new files only\03.02\a\20\vrd#1@1.csv');

Rsfw_20_a=(F_data{1,3}-F_data{46,3})/(F_data{1,2}-F_data{46,2})

Rsrv_20_a=(F_data{225,3}-F_data{280,3})/(F_data{225,2}-
F_data{280,2})
```

```
G_data = dataset('xlsfile','E:\Continuation_MSc thesis\backup\backup
03.02 new files only\03.02\a\17\vrd#1@1.csv');

Rsfw_17_a=(G_data{1,3}-G_data{46,3})/(G_data{1,2}-G_data{46,2})

Rsrv_17_a=(G_data{225,3}-G_data{280,3})/(G_data{225,2}-
G_data{280,2})

H_data = dataset('xlsfile','E:\Continuation_MSc thesis\backup\backup
03.02 new files only\03.02\a\15\vrd#1@1.csv');

Rsfw_15_a=(H_data{1,3}-H_data{46,3})/(H_data{1,2}-H_data{46,2})

Rsrv_15_a=(H_data{225,3}-H_data{280,3})/(H_data{225,2}-
H_data{280,2})

I_data = dataset('xlsfile','E:\Continuation_MSc thesis\backup\backup
03.02 new files only\03.02\a\12\vrd#1@1.csv');

Rsfw_12_a=(I_data{1,3}-I_data{46,3})/(I_data{1,2}-I_data{46,2})

Rsrv_12_a=(I_data{225,3}-I_data{280,3})/(I_data{225,2}-
I_data{280,2})

J_data = dataset('xlsfile','E:\Continuation_MSc thesis\backup\backup
03.02 new files only\03.02\a\10\vrd#1@1.csv');

Rsfw_10_a=(J_data{1,3}-J_data{46,3})/(J_data{1,2}-J_data{46,2})

Rsrv_10_a=(J_data{225,3}-J_data{280,3})/(J_data{225,2}-
J_data{280,2})

K_data = dataset('xlsfile','E:\Continuation_MSc thesis\backup\backup
03.02 new files only\03.02\a\8\vrd#1@1.csv');

Rsfw_8_a=(K_data{1,3}-K_data{46,3})/(K_data{1,2}-K_data{46,2})

Rsrv_8_a=(K_data{225,3}-K_data{280,3})/(K_data{225,2}-K_data{280,2})

L_data = dataset('xlsfile','E:\Continuation_MSc thesis\backup\backup
03.02 new files only\03.02\a\7\vrd#1@1.csv');

Rsfw_7_a=(L_data{1,3}-L_data{46,3})/(L_data{1,2}-L_data{46,2})

Rsrv_7_a=(L_data{225,3}-L_data{280,3})/(L_data{225,2}-L_data{280,2})

M_data = dataset('xlsfile','E:\Continuation_MSc thesis\backup\backup
03.02 new files only\03.02\a\6\vrd#1@1.csv');

Rsfw_6_a=(M_data{1,3}-M_data{46,3})/(M_data{1,2}-M_data{46,2})

Rsrv_6_a=(M_data{225,3}-M_data{280,3})/(M_data{225,2}-M_data{280,2})

N_data = dataset('xlsfile','E:\Continuation_MSc thesis\backup\backup
03.02 new files only\03.02\a\5\vrd#1@1.csv');
```

```
Rsfw_5_a=(N_data{1,3}-N_data{46,3})/(N_data{1,2}-N_data{46,2})

Rsrv_5_a=(N_data{225,3}-N_data{280,3})/(N_data{225,2}-N_data{280,2})

O_data = dataset('xlsfile','E:\Continuation_MSc thesis\backup\backup
03.02 new files only\03.02\a\4\vrd#1@1.csv');

Rsfw_4_a=(O_data{1,3}-O_data{46,3})/(O_data{1,2}-O_data{46,2})

Rsrv_4_a=(O_data{225,3}-O_data{280,3})/(O_data{225,2}-O_data{280,2})

P_data = dataset('xlsfile','E:\Continuation_MSc thesis\backup\backup
03.02 new files only\03.02\a\3\vrd#1@1.csv');

Rsfw_3_a=(P_data{1,3}-P_data{46,3})/(P_data{1,2}-P_data{46,2})

Rsrv_3_a=(P_data{225,3}-P_data{280,3})/(P_data{225,2}-P_data{280,2})

Q_data = dataset('xlsfile','E:\Continuation_MSc thesis\backup\backup
03.02 new files only\03.02\a\2\vrd#1@1.csv');

Rsfw_2_a=(Q_data{1,3}-Q_data{46,3})/(Q_data{1,2}-Q_data{46,2})

Rsrv_2_a=(Q_data{225,3}-Q_data{280,3})/(Q_data{225,2}-Q_data{280,2})

R_data = dataset('xlsfile','E:\Continuation_MSc thesis\backup\backup
03.02 new files only\03.02\a\1\vrd#1@1.csv');

Rsfw_1_a=(R_data{1,3}-R_data{46,3})/(R_data{1,2}-R_data{46,2})

Rsrv_1_a=(R_data{225,3}-R_data{280,3})/(R_data{225,2}-R_data{280,2})
```

Appendix G

The calculation of the number of the spots is made with the software ImageJ and the “Find Maxima” option after applying a median filter on the image. This technique applies for diodes with a diameter >10µm where it is possible to discriminate the spots by naked eye. For diodes with a diameters <10µm where a single spot appears, a different technique is used where the number of spots is approximately the ratio of the Area of the diode over the Area of the first little spot appearing in the measurement for low bias.

References

[1] N. ROGER, “Visible Light from a Silicon p-n Junction,” *Physical Review*, vol. 100, no. 2, Oct. 1955.

[2] M. Morschbach, M. Oehme, and E. Kasper, “Visible Light Emission by a Reverse-Biased Integrated Silicon Diode,” *IEEE TRANSACTIONS ON ELECTRON DEVICES*, vol. 54, no. 5, May 2007.

[3] L. Qi, K. R. C. Mok, M. Aminian, E. Charbon, and L. K. Nanver, “Fabrication of Low Dark-Count PureB Single-Photon Avalanche Diodes,” presented at the Microelectronics Technology and Devices (SBMicro), 2014 29th Symposium on Microelectronics Technology and Devices, Aracaju - Sergipe - Brazil, 2014.

[4] L. Qi, K. R. C. Mok, M. Aminian, E. Charbon, and L. K. Nanver, “UV-Sensitive Low Dark-Count PureB Single-Photon Avalanche Diode,” IEEE TRANSACTIONS ON ELECTRON DEVICES, vol. 61, no. 11, Nov. 2014.

[5] http://www.cs.utexas.edu/users/EWD/transcriptions/EWD00xx/EWD74.html

[6] A. Silberschatz, P. Baer Galvin, and G. Gagne, “5.6 Semaphores,” in *Operating Systems Concepts*, 9th ed., United States of America: Wiley, 2013.

[7] A. S. TANENBAUM, “2.3 INTERPROCESS COMMUNICATION,” in *MODERN* OPERATING SYSTEMS, 3rd ed., Amsterdam, The Netherlands: PEARSON, 2009.

[8] http://windows.microsoft.com/en-us/windows7/products/features/windows-xp-mode

[9] Keithley 4200 SCS reference manual (code: 4200-901-1)

[10] XenICs XEVA model manual (chapter 1 - Introduction)

[11] http://www.edmundoptics.com/microscopy/infinity-corrected-objectives/mitutoyo-nir-nuv-uv-infinity-corrected-objectives/46405/

[12] http://www.ioffe.ru/SVA/NSM/Semicond/Si/bandstr.html

[13] S. S. Iyer and Y.-H. Xie, “Light Emission from Silicon,” Science, New Series, vol. 260, no. 5104, pp. 40–46, Apr. 1993.

[14] M. A. Green and M. J. Keevers, “Optical Properties of Intrinsic Silicon at 300 K,” PROGRESS IN PHOTOVOLTAICS: RESEARCH AND APPLICATIONS, vol. 3, pp. 189–192, 1995**.**

[15] J. R. Haynes and W. C. Westphal, “Radiation Resulting from Recombination of Holes and Electrons in Silicon,” Physical Review, vol. 101, no. 6, Mar. 1956.

[16] S. Dutta, R. J. E. Hueting, A.-J. Annema, L. Qi, and L. K. Nanver, “Opto-electronic modeling of light emission from avalanche-mode silicon p+n junctions,” Journal of Applied Physics, vol. 118, no. 114506, 2013.

[17] J. H. Swoger and S. J. Kovacic, “Enhanced luminescence due to impact ionization in photodiodes,” vol. 74, no. 2565, 1993.

[18] J. Kramer, P. Seltz, H. Auderset, B. Delley, and H. Baltes, “Light-emitting devices in industrial CMOS technology,” Sensors and Actuators A, vol. 37–38, pp. 521–533, 1993.

[19] A. G. Chynoweth and G. L. Pearson, “Effect of Dislocations on Breakdown in Silicon pn Junctions,” Journal of Applied Physics, vol. 29, no. 1103, 1958.

[20] M. Morschbach, M. Oehme, J. Werner, and E. Kasper, “Visible to Infrared Light Emission from Reverse Defect Engineered Silicon Junctions,” presented at the 5th International Conference on Group IV Photonics, GFP, Sorrento, Italy, 2008, pp. 32–34.

[21] J. Bao, M. Tabbal, T. Kim, S. Charnvanichborikarn, J. S. Williams, M. J. Aziz, and F. Capasso, “Point defect engineered Si sub-bandgap light-emitting diode,” Optics Express, vol. 15, no. 11, pp. 6727–6733, May 2007.

[22] B. Schippers, “Dislocation engineered silicon Light Emitting Diode,” MSc thesis, University of Twente, Enschede, The Netherlands, 2005.

[23] A. T. FIORY and N. M. RAVINDRA, “Light Emission from Silicon: Some Perspectives and Applications,” Journal of ELECTRONIC MATERIALS, vol. 32, no. 10, 2003.

[24] E. Ö. Sveinbjörnsson and J. Weber, “Room temperature electroluminescence from dislocation-rich silicon,” Applied Physics Letters, vol. 69, no. 18, pp. 2686–2688, Oct. 1996.

[25] L. W. Snyman, H. Aharoni, M. du Plessis, and R. B. J. Gouws, “Increased efficiency of silicon light-emitting diodes in a standard 1.2-um silicon complementary metal oxide semiconductor technology,” Opt. Eng., vol. 37, no. 7, pp. 2133–2141, Jul. 1998.

[26] T. Hoang, “High Efficient Infrared Light Emission from Silicon LEDs,” PhD thesis, University of Twente, Enschede, The Netherlands, 2007.

[27] W. Lek Ng, M. A. Lourenco, R. M. Gwilliam, S. Ledain, G. Shao, and K. P. Homewood, “An efficient room-temperature silicon-based light-emitting diode,” Nature, vol. 410, pp. 192–194, 2001.

[28] A. G. CHYNOWETH and K. G. MCKAY, “Photon Emission from Avalanche Breakdown in Silicon,” Physical Review, vol. 102, no. 2, Apr. 1956.

[29] N. Akil, S. E. Kerns, D. V. Kerns Jr., A. Hoffmann, and J.-P. Charles, “Photon generation by silicon diodes in avalanche breakdown,” Applied Physics Letters, vol. 73, no. 871, 1998.

[30] L. Minh Phuong, “Silicon Light Emitting Devices for Integrated Applications,” Ph.D. thesis, University of Twente, Enschede, The Netherlands, 2003.

[31] K. D. Hirschman, L. Tsybeskov, S. P. Duttagupta, and P. M. Fauchet, “Silicon-based visible light emitting devices integrated into microelectronic circuits,” Nature, vol. 384, Nov. 1996.

[32] J. SHEWCHUNT and L. Y. WE1, “MECHANISM FOR REVERSE-BIASED BREAKDOWN RADIATION IN p-n JUNCTIONS,” Solid-State Electronics, vol. 8, pp. 485–493, 1965.

[33] D. V .Kerns, K. Arora, S. Kurinec, and W. Power, “SI DIODE UNDER AVALANCHE BREAKDOWN AS A LIGHT EMITTING SOURCE FOR VLSI OPTICAL INTERCONNECT,” in System Theory, Tallahassee, FL, 1989, pp. 677 – 680.